Hybrid Energy Harvesting for Self Powered Human Applications

Boris Karajica

A Thesis

in

The Department

of

Electrical and Computer Engineering

Presented in Partial Fulfillment of the Requirements

for the Degree of Master of Applied Science at

Concordia University

Montréal, Québec, Canada

March 2013

CONCORDIA UNIVERSITY

School of Graduate Studies

This is to certify that the Thesis prepared

By: Boris Karajica I.D. 6110827

Entitled: "Hybrid Energy Harvesting for Self Powered Human Applications"

and submitted in partial fulfillment of the requirements for the degree of

Master of Applied Science

complies with the regulations of the University and meets the accepted standards with respect to originality and quality.

Signed by the final examining committee:

Prof. Samar Abdi _____ Chair

Prof. Zahangir Kabir _____Examiner

Prof. Muthukumaran Packiris _____ Examiner

Prof. Sheldon Williamson _____ Supervisor

Approved by _____

Chair of Department or Graduate Program Director

_____

Dean of Faculty

Date _____

ABSTRACT

Hybrid Energy Harvesting for Self Powered Human Applications

Boris Karajica

Continuing progress in reduction of size and power consumption of semiconductors, and significant improvement in their capability to compute sense and communicate data, have enabled a new area of wearable electronics and smart garments. Mobile electronics devices such as smart phones, tablets, laptops, e-readers and GPS devices have shaped and defined the world of consumer electronics. As such those devices interact with us on every day level, keeping us connected with environment through the use of sensors, imagers, location based services and data networks. Looking beyond typical consumer applications, there is an increasing demand for a wearable and energy efficient electronics capable of operating from human harvested energy. This study will present a solution that is capable of providing basic human bio-parametric data such as: body temperature, pressure, man down indication, impact occurrence indication as well as data on orientation and inclination. All those functions will be embedded as wearable electronics and be able to operate from the energy that was harvested from human body. The need to have this kind of data collected on the human subject in especially demanding environments and situations is greatly appreciative in applications related to search and rescue agencies, paramedics, firefighters and security and police. The solution presented in this thesis is focusing on energy harvesting from human body and the environment, together with utilization of such energy for wearable electronics.

ACKNOWLEDGMENTS

This thesis would not have been possible without the help and support of many people to whom I would like to express my gratefulness. In the first place, I would like to thank my advisor Professor Dr. Sheldon Williamson. Your constant support, patience and inspiration were always very motivating, and many fruitful discussions inspired much of the work presented in this thesis. I have benefited a lot from your experience and I am very glad that I got the chance to join your research group. I would also like to express my gratitude to Professors: Dr. Samar Abdi, Dr. Zahangir Kabir and Dr. Muthukumaran Packirisamy for being my co-examiners. Thanks for investing the time to read through the thesis. I thank all my current and former colleagues of the PEER group for their company and support.

TABLE OF CONTENTS

LIST OF FIGURES

LIST OF TABLES

LIST OF ACRONYMS

Ah	Ampere-Hour
ADC	Analog to digital converter
α	Inclination angle with respect to the earth's surface
BaTiO3	Barium Titanate
β	Inclination angle with respect to sun
CD	Charge Depleting
CAN	Ultra robust communication bus available on microcontroller
CS	Control Strategy
CH4	Methane
DAC	Digital to analog converter
DH	Daylight hours
d31	direction of impact force on piezoelectric element
E-Jacket	Sport utility garment equipped with embedded electronics
EEPROM	Electrically erasable programmable memory
E	Energy
ESS	Energy Storage System
FLASH	Non-volatile memory device that can be reprogrammed
GA	Genetic Algorithm
GPS	Global Positioning System
I2C	Multi-master serial single-ended bus invented by Philips
I/O	Digital Input/output port
	Current generated by the cell as a result of the light radiating on the cell
Id	Reverse saturation current of the diode

Ip	Leakage current to the ground
LED	Light emitting diode
MCU	Microcontroller unit
MEMS	Micro-electro-mechanical system
MPP	Maximum Power Point
mr	Thermal load resistance ratio
K	Boltzman constant
NFC	Near filed communication radio
PV	Photovoltaic element
RF	Radio frequency
RTEG	Electrical resistance of TEG
RFNFC	13.56MHz radio utilized for neared field communication
θz	Resultant angle of inclination with respect to time of the day and location
Q	Electrical charge
STM32L	32-bit ultra-low power microcontroller
SPI	Serial Peripheral Interface Bus
SDIO	Secure digital Interface
SRAM	Static random access memory
TEG	Thermo-electrical generator
VMPP	Maximum power point voltage

CHAPTER 1

1.0 INTRODUCTION

Human kind through its existential development and survival has placed an enormous effort on extracting, making and transforming energy for the purpose of survival and evolution [1]. Energy has had and will continue to have a pivotal role in human existence. All the indicators are showing that human kind is migrating from the concept of making the energy into a concept of harvesting the energy. Human body is not only an energy consumer but an energy generator as well. There are significant challenges not only in harvesting the energy, but also in converting the energy into useful and stable power. This thesis examines the ways that energy can be harvested from the human body and the surroundings, thus relaying on both the nature and the human body as an energy sources [2]. The power conversion techniques that can generate stable and continuous power are examined as well. This thesis deals with the idea of harvesting the human energy for the purpose of providing an alternative power supply for an E-jacket. The concept of E-jacket is summarized in a garment that has embedded sensors: temperature sensor, accelerometer, digital magnetometer and pressure sensor. Those sensors are powered by the motion of the person that is wearing a jacket as well as from the body heat and solar sources from the outside environment. Each sensor is providing an integrated type of information related to the environment and the subject that is wearing an E-jacket. Motion performed during walking generates energy at the elbow and at the shoulder joints, as well as heat which is released as a result of work done by the body [3]. During these phases of motion and torque, a breaking force can be replaced by an electrical generator. Heat emitted by human body can be harvested by the thermal energy harvesters [4]. The ambient

energy from the surroundings -sunlight is harvested as well through the use of organic flexible PV panels [5]. Harvested energy is utilized the power a range of functional features within the E-jacket, such as: man down sensor (combination of 3-axis digital accelerometer + 3-axis digital gyroscope), digital thermometer for body temperature, pressure sensor for elevation detection and digital compass for orientation. All the above obtained parametric measurements are stored in 128MB of EEPROM memory with dual interface: RF-NFC (near field communication-RF) and digital (I^2C). The obtained and stored data is then periodically transferred to a mobile phone or a hand held radio via low power near filed communication protocol- NFC. The proposed solution is represented in a block diagram in Fig. 1-1

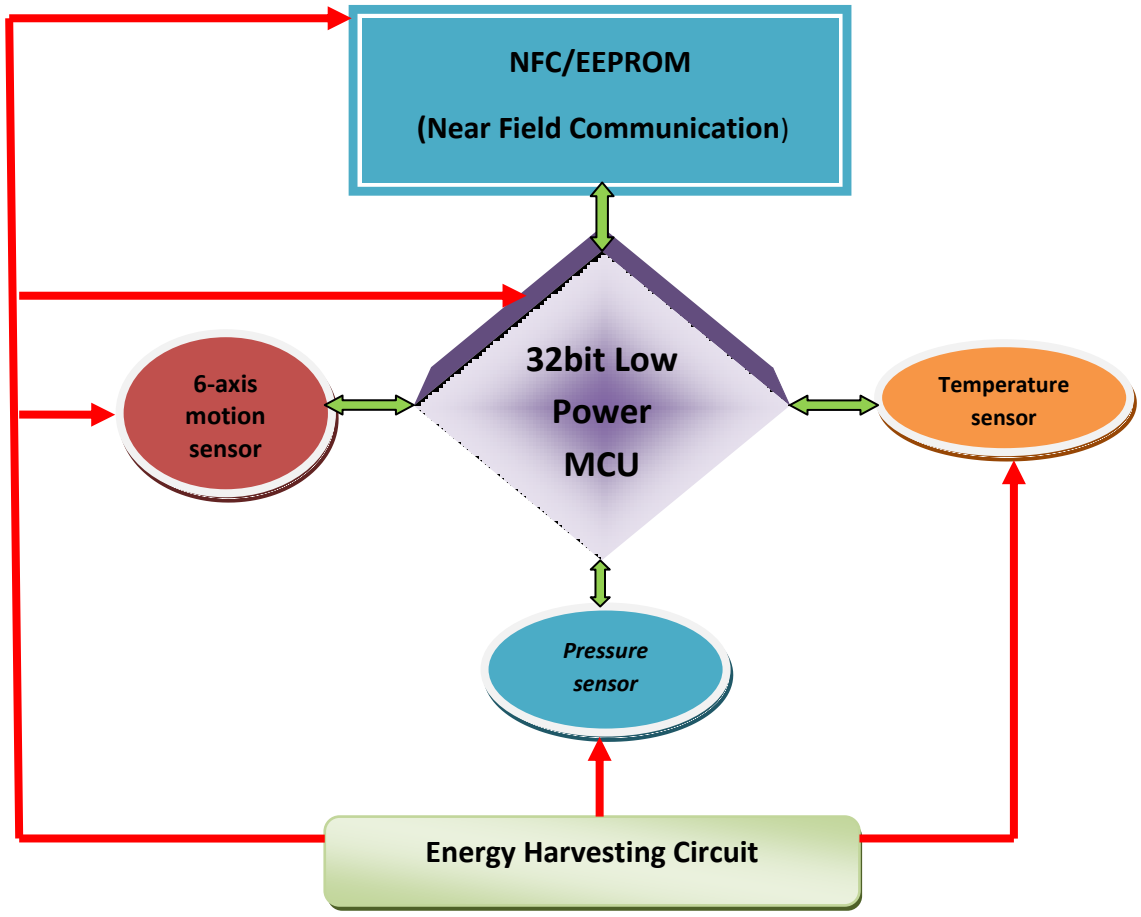

Fig.1- 1 System overview of integrated sensor and power solution for E-Jacket

Energy is extracted from the following: body heat, limb and joint motion, vibration generated by the movement of the body and light/solar energy from the environment.

Energy Transducer or energy harvesting generator is a device used to collect and convert the available energy into electrical energy. In the case of this study, energy transducers that are benign used are the following: piezoelectric elements, thermal generators and flexible mini PV panels. As an energy storage element, a thin film battery has been selected due to its small form factor as well as its robustness and high number of charge and discharge cycles. Energy harvesting circuit consists of power rectifier that is converting AC acquired power from energy harvesting devices and is converting it into a DC power. Voltage regulator is also part of energy harvesting circuit and has a purpose to adopt the voltage levels to the requirements of the devices that need to be powered.

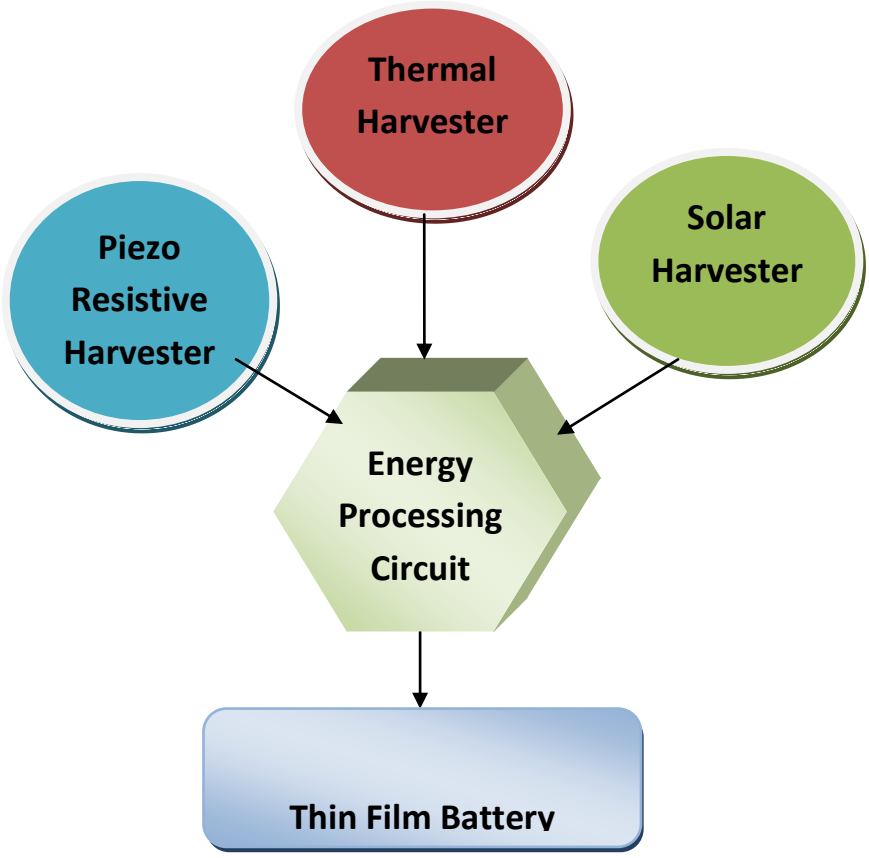

Fig.1- 2 Block diagram of Energy Harvesting system

1.1 FUNCTIONALITY OVERVIEW

This section will take a closer look into functionality and performance of each subsystem and its components used in a design of an E-jacket application. There are six major components that define overall functionality and performance of E-Jacket. Those components can be grouped into four subsystems: energy converters, energy storage, sensors, radio link and digital control unit. In the design of the overall system particular focus has been placed on implementation of low power functions for sensor subsystems. Utilization of sleep and power down modes on digital control unit-microcontroller was essential in accomplishing reduced power consumption and prolonged battery life. More detailed overview of power conversation will be presented in the following chapters.

1.2 MICROCONTROLLER – STM32L

This is an ultra-low power 32-bit microcontroller based on ARM's Cortex M3 core designed and manufactured in ST's 90nm CMOS process. The MCU runs at 36 MHz maximum frequency, 1.25 DMIPS/MHz (Dhrystone 2.1) performances at 0 wait state memory access [6]. It performs single-cycle multiplication and hardware division. Instruction set is Thumb II, which makes the whole solution very and low power. STM32L has multiple power modes ranging from 190uA-0.4uA (Fig. 1-3): dynamic RUN from flash, dynamic RUN from RAM, low power run, low power wait and active halt [8]. Supply voltage is ranging from 1.8V-3.6V. In its optimum configuration the MCU can have up to 512 Kbytes of Flash memory and 64 Kbytes of SRAM. It has built in 3x12 bit ADC and 2x12bit DAC. The following interfaces are available: I^2C, 3 SPI, CAN, USB and SDIO(secure digital interface). Interrupt-based firmware development is highly encouraged in embedded systems, and Cortex-M processors are equipped with a nested vectored interrupt controller (NVIC) to

enhance the processor's interrupt handling capabilities. As the name suggests, the address of the function to be executed (also known as the interrupt handler) is stored in a vector table, and the processor refers to the table when an interrupt has taken place **Error! Reference source not found.**.

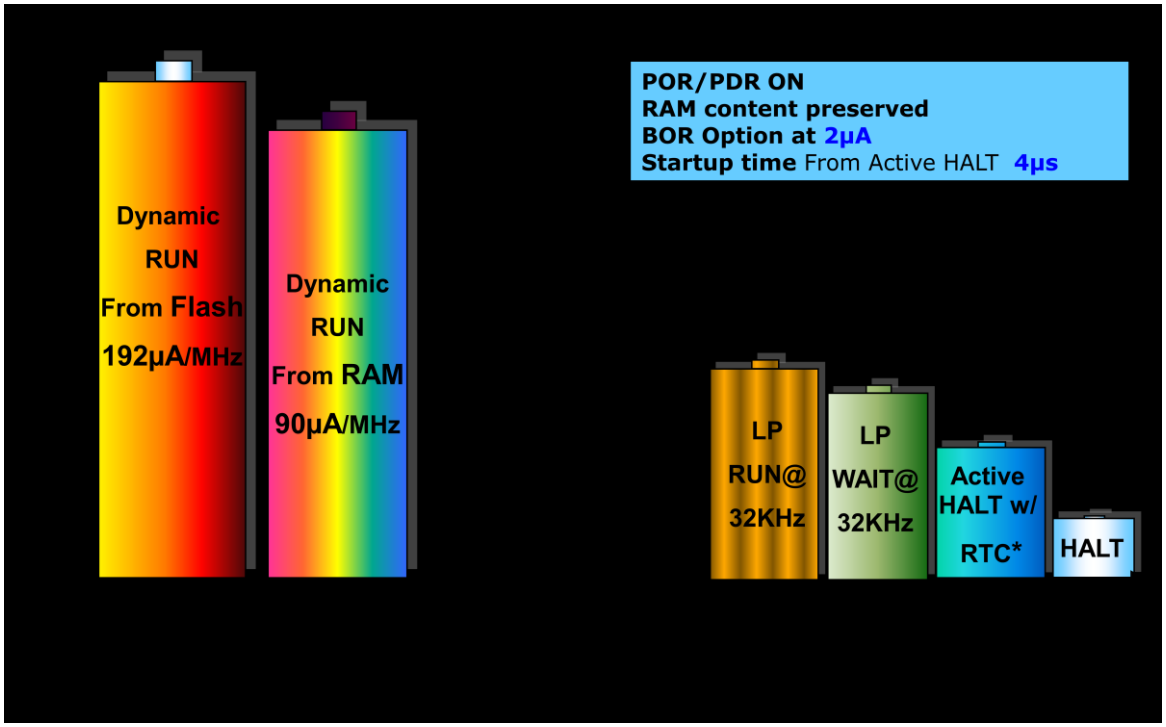

Fig.1- 3 Different power modes for STM32L

1.3 SENSOR FUNCTIONS OVERVIEW

Sensors provide man-down, impact detection, inclination, temperature and orientation features for the E-Jacket application. Five different low power sensors are used in this study, out of five sensors used; three are motion based sensors (accelerometer, gyroscope and magnetometer). In addition to motion, additional two (pressure and temperature sensors) provide environmental data. The inner workings of the sensors are based on the ability of analog/digital electronics to "understand" the data stream out of the mechanical structure of sensors [9]. The system level of sensor functionality is presented in Fig. 1-4.

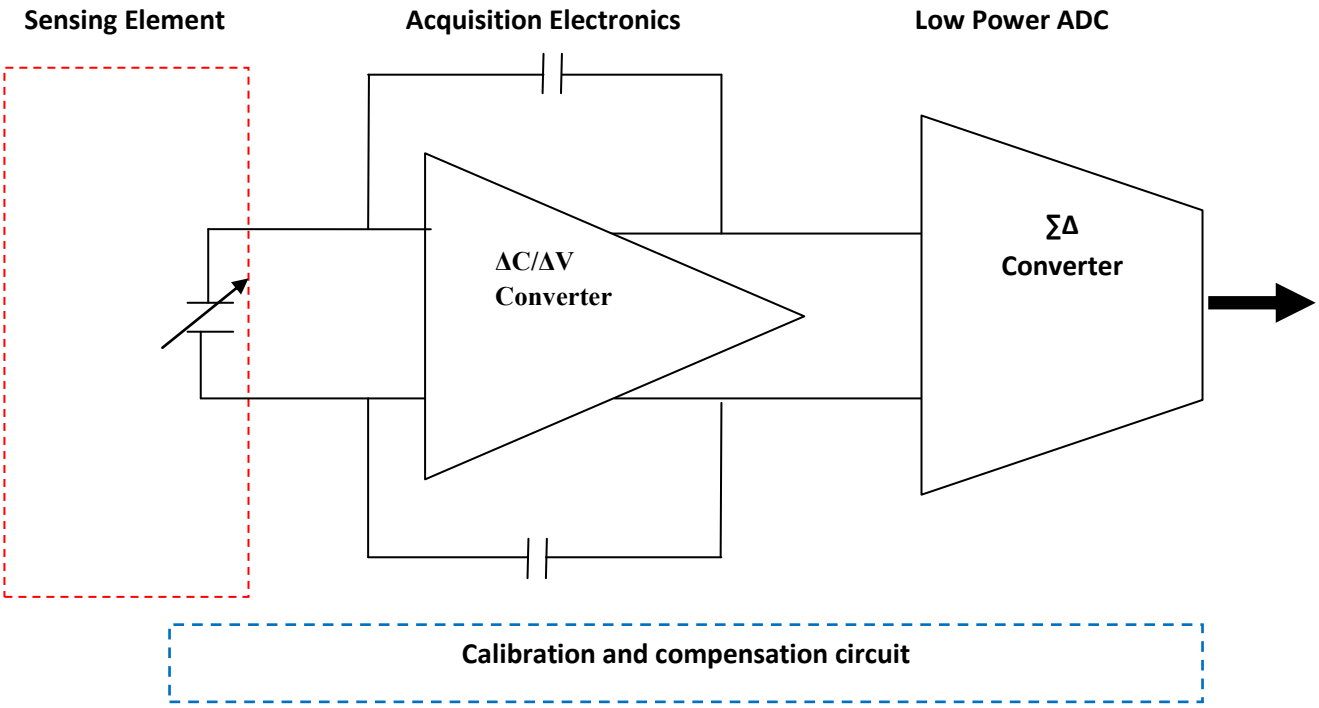

Fig.1- 4 Block diagram for capacitive bases pressure sensor

1.3.1 ACCELEROMETER

Accelerometers measures linear acceleration as long as there is no rotation [10]. When the device is rotated, the acceleration of gravity is measured as well and there is no way to distinguish with the linear motion (Fig. 1-5).

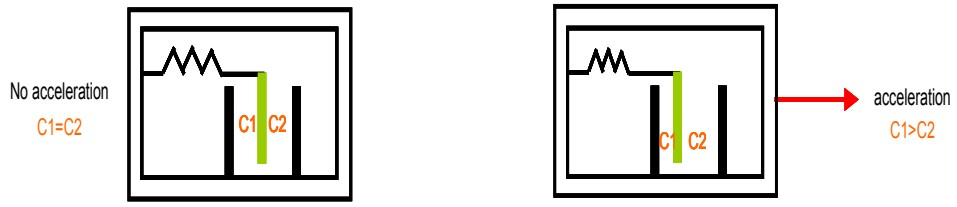

Fig.1- 5 Directional interpretation of linear acceleration

Accelerometer can be used to sense orientation, vibration, shock, tilt and free fall. There are a number of general measurement requirements that must be dealt with in measuring any transient signal that has an important time-history. The data sampling rate must be at least twice the highest data frequency of interest. Properly selected data filters must constrain data signal content, so that data doesn't exceed this highest frequency. If significant high frequency content is present in the signal, and its time history is of interest, data sampling should occur at 10 times this highest frequency. The data must be validated to have an adequate signal to noise ratio. Key parametric features of the 3-axis digital accelerometer are presented in Table 1-1.

Table 1- 1 Functionality fearers of 3-axis digital accelerometer

Supply Voltage	1.8V-3.6V
Low voltage compatible IOs	1.6V
Ultra low-power mode consumption	10uA
Dynamically selectable full scale	±2g/±4g/±8g
Digital output interface	I^2C/SPI
Output data resolution	16 bit
Selectable sensitivity levels	1 mg/digit @ ±2g; 2 mg/digit @ ±4g;
Output data rate	0.5Hz to 1KHz
Free fall and motion detection	2 programmable interrupt generators

Accelerometer devices are composed of mechanical part (sensing part) and ASIC interface (analog/digital interface to mechanical structures). Fig. 1-6 shows a picture of inner workings of the accelerometer [11].

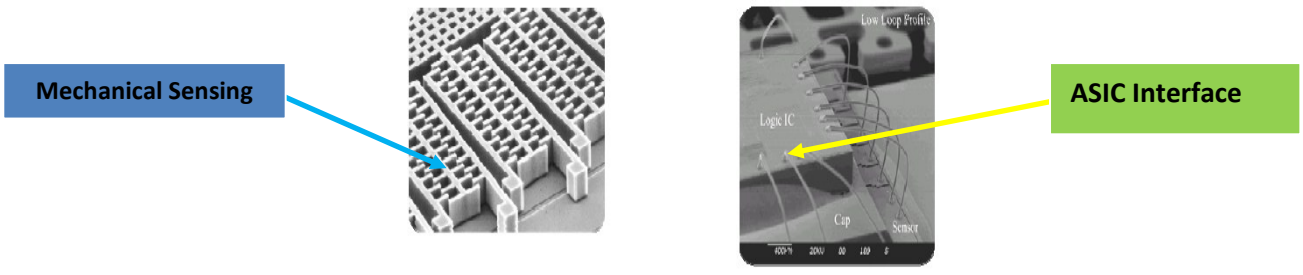

Fig.1- 6 Snapshot of the MEMS accelerometer die

1.3.2 GYROSCOPE

Gyroscope is a MEMS sensor MEMS that converts Input Signal (Angular Rate) in a Differential Capacitive Change, based on the Coriolis apparent acceleration that arises in a rotating reference frame. Gyroscopes measure the angular rate of rotation [12]**.** Fig 1-7 presents block diagram of the physical concept behind the Coriolis force.

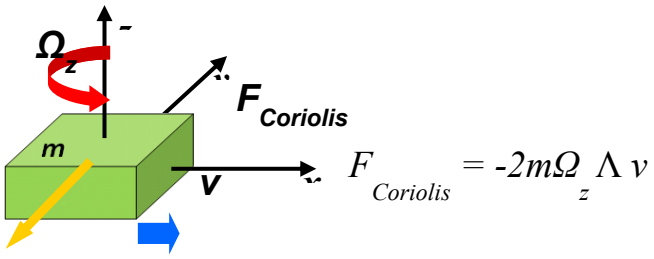

Fig.1- 7 Coriolis force and its effect on object with mass m

Gyroscope structures manufactured in MEMS process have a single sensing structure for motion measurement along all three orthogonal axes. When the device is rotated, the sensor detects the movements while linear displacements are not measured as illustrated in Fig 1-8.

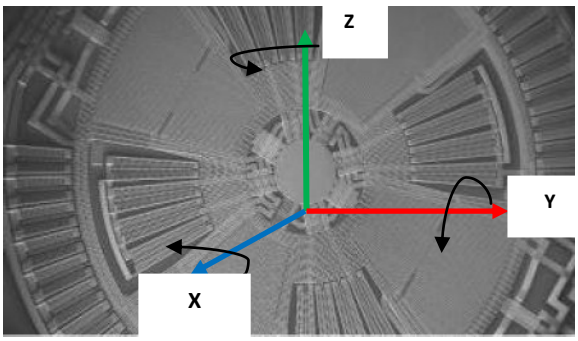

Fig.1- 8 Gyroscope structure manufactured in MEMS process

3-axis digital gyroscope is interfaced with low power (STM32L) microcontroller through I^2C. Gyroscope together with digital accelerometer provides 6- axis of data acquisition which are processed in real time by STM32L and based on data it is determined if the man-down or impact has occurred. Utilization of a gyroscope is optimized through the use of low power

states as well as build- in state machines with pre-set interrupt controller. Key features considered for utilization of 3-axis digital gyroscope are presented in Table 1-2.

Table 1- 2 Performance characteristics of L4G4200D

Operating Voltage	1.8V-3.6V
Temperature Range	(-40°C to +85°C)
Sensitivity	3.33 mv/ °/s @ ±300 °/s or 0.83 mv/ °/s @ ±1200 °/s
Dual Axes pitch and roll (pitch and yaw)	±300 °/s (4x) or ±1200 °/s (1x)
Output Amplification	Two separated outputs for each axis (1x an 4x amplified)
Embedded features	Integrated low pass filter; power down
Data Output	16-bit
Output Interfaces	I^2C/SPI digital output interface

1.3.3 MAGNOTEMETER

Magnetometer is a MEMS type of device that is able to measure the intensity of the magnetic field and based on that information system is able to determine a position of the sensor in respect to magnetic north [13]. In E-jacket application magnetometer is used to determine magnetic north and to assist accelerometer and gyroscope in more precisely determining if the subject is moving or the man-down event has occurred. The overall fusion of sensor data is handled by microcontroller with sensor fusion algorithm integrated in it. Key features of digital magnetometer are summarized in Table 1-3.

Table 1- 3 Digital magnetometer key features

Operating Voltage	1.8V-3.3V
Dimensions	4.0 x 4.0 x 1.3mm Low Height Profile
Interface	I^2C
Magnetic Range	±4 Ga
Programmable sensitivity	±0.7 Gaup to ±4 Ga
Programmable output data rate	0.5 Hz up to 50 Hz
Bandwidth	10KHz

1.3.4 PRESURE SENSOR

Capacitive MEMS pressure sensor used in E-Jacket application is able to provide the function of a barometer and a function of an inclinometer as well. The data coming out of the pressure senor is read by the microcontroller and with software look up table it can be determined what is the inclination and barometric pressure at that inclination [14]. Pressure sensor is based on capacitive sensing element, voltage conditioning circuit and clocking circuit. Block diagram of capacitive pressure sensor is presented in Fig. 1-9.

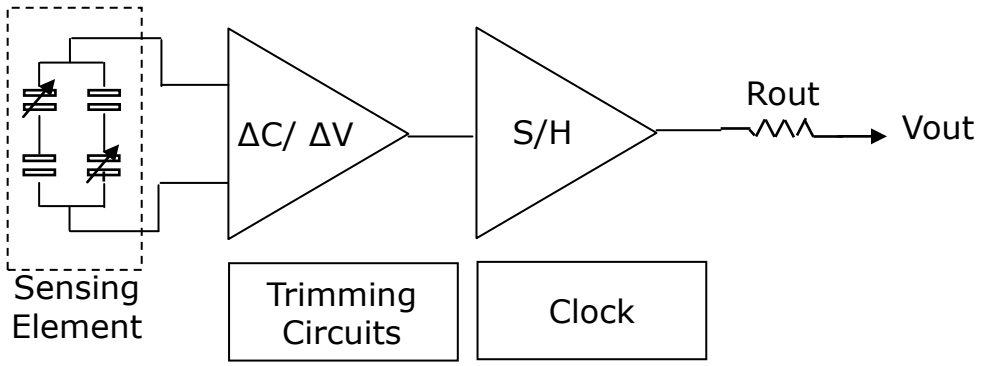

Fig.1- 9 Block diagram of capacitive pressure sensor

Table 1- 4 Pressure sensor operating characteristics

Supply Voltage	2.4V-3.6V
Pressure range	0-50mbar
Accuracy	0.5mbar
Temperature Range	-0.25^0C to 85^0C
Output data resolution	16bit
Digital Interface	I^2C and SPI

1.4 DUAL INTERFACE 128Kb EEPROM MEMORY

Dual Interface EEPROM is a memory device based on flash process [16]. The device is capable of sending and receiving the data via RF and I2C interface. It is also capable of

receiving the power wirelessly through RFID like interface operating at 13.56MHz. System level representation is shown in Fig.1-10.

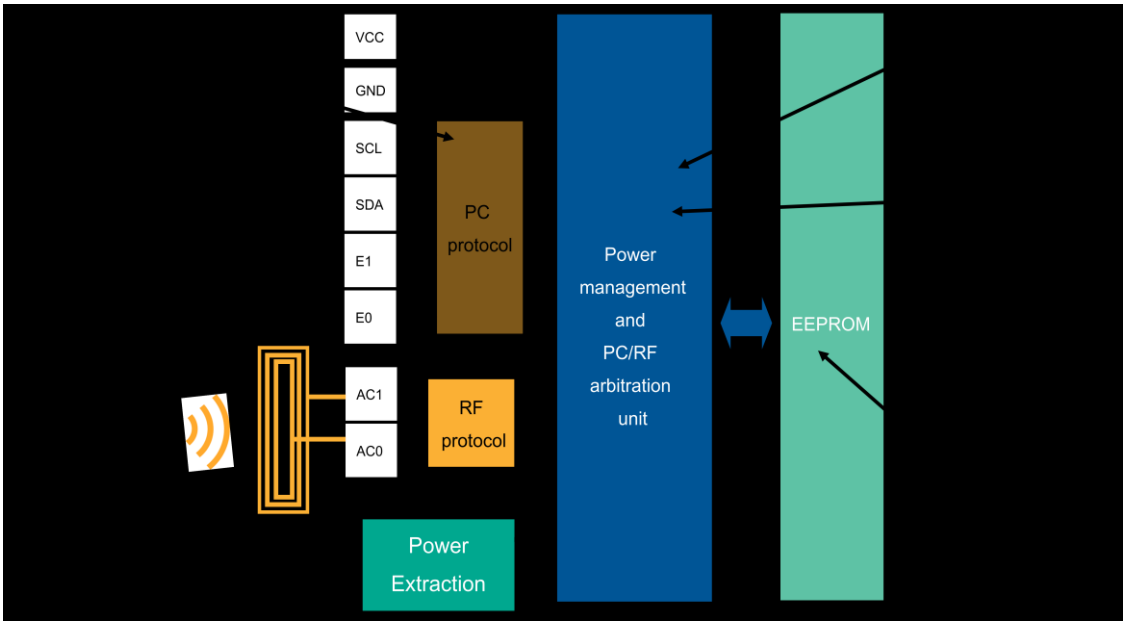

Fig.1- 10 Block diagram of M24LR128 dual interface EEPROM

When supplied only from the RF side: the M24LR128 can be accessed only by the RF reader, and when supplied only from VCC, M24L128 can be accessed only by the I²C interface. If supplied from both the VCC pin and the RF field: M24LR128 will apply an internal ready/busy flag and serve the first decoded command (either RF or I²C) and will not decode any command from the other interface (either I²C or RF) until the first decoded command is complete. Table 1-5 contains all the key operation parameters of M24LR128

Table 1- 5 Operational features of M24LR128

Operating Voltage	1.8V – 5.5V
RF Interfaces	ISO15693 & ISO 18000
Digital Interface	I^2C
Memory Capacity	128Kb EEPROM
Write Time	I^2C @ 5ms; RF @ 5.75ms
Data Retention	40 years
Write Cycles	1 million

1.5 E-JACKET FUNCIONALITY AND ENERGY HARVESTING

E-Jacket function is intended for search and rescue teams, firefighters, ambulance personal and police and security. Another very important application for an e-jacket is for sports and recreation. The idea is to develop a wearable smart platform that can provide a general feedback to the user about the surrounding environmental conditions and also provide the feedback on the condition of the user well [17]. The E-Jacket is equipped with five different sensors: accelerometer, gyroscope, magnetometer, pressure sensor and temperature sensors. All of the sensors have digital interface and are connected to the microcontroller (STM32L) via I^2C or SPI interfaces [18]. Overall system is able to function from 1.8V supply voltage. The data collected by the sensors is stored in dual interface EEPROM memory and it can be transferred to a mobile phone equipped with NFC reader. E-Jacket is able to provide the following information: linear acceleration as well as “man down” event (this is done with accelerometer), geo-positional heading (magnetometer), barometric pressure and inclination (pressure sensor), external temperature and body temperature (temperature sensor) [20]. All the sensors are event driven and have a capability to send an interrupt to the MCU (microcontroller), which means that all the digital devices including the MCU can be put to ultra-low power sleep mode and woken up by external interrupt such as motion or a fall or low temperature threshold [21].

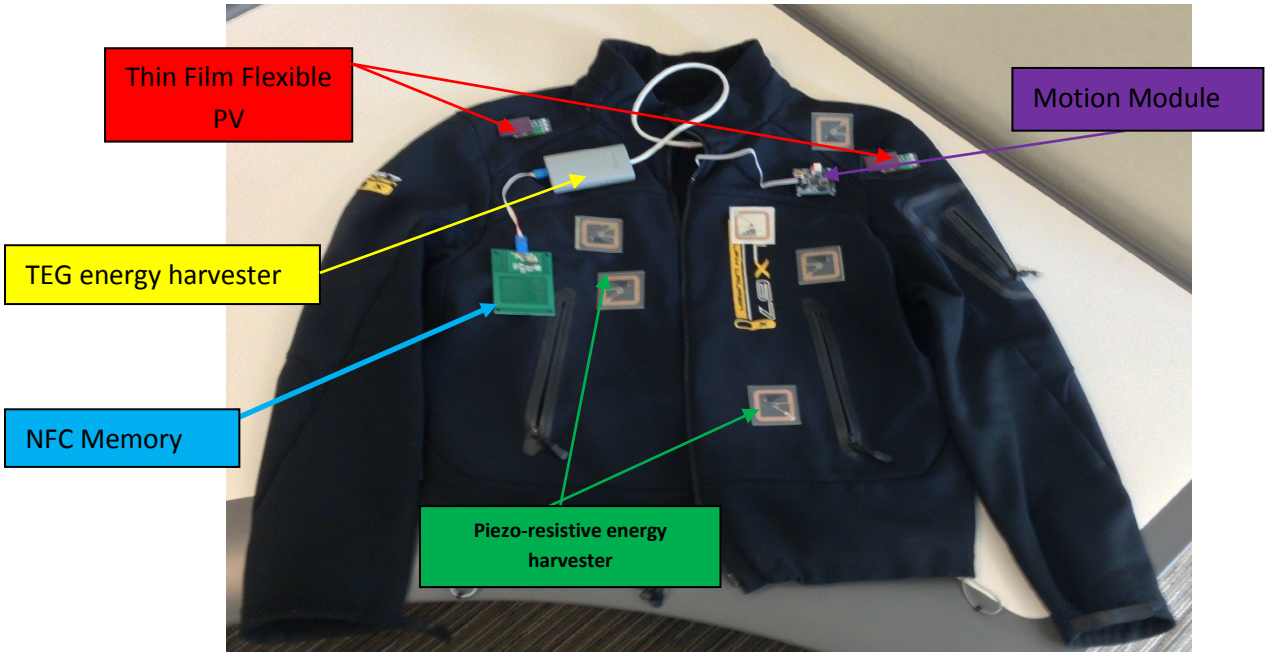

Fig.1- 11 E-Jacket prototype with location indicator for each function

Special considerations had to be taken in understanding where is the most optimum location on human body to place the energy harvesters, sensors, radio and energy storage (Fig. 1-10). Energy harvesters have to be placed on a location that will provide the most optimum MPPT (maximum power transfer of energy) [22]. In a case of TEG harvester it is important to place on the locations of the body that dissipate heat the most, which means area of the upper body that have the highest concentration of blood vessels. Those areas are head (hood of the E-jacket), frontal part of the hood (mouth piece) chest (front of the jacket) and bellow the armpit (between the sleeves and the side of the body). Piezoelectric energy harvester needs to place in the area which is exposed to most of the upper body motion [37]. Those areas are around the elbows and shoulder pads. Thin film flexible PV's are the most significant source of energy and they are the easiest to install, maintain and they have the lowest cost/ W of power produced. PVs will be placed on the side of the sleeves, large portion of the back and frontal area. The storage elements will be based on thin film batteries. They exhibit certain

properties that are very suitable for wearable electronics such as: small form factor, their flexible structure and robustness. They also have very flexible capacity, mining that by stacking them together, the overall storage capacity can be increased. Output of a relatively active adult body is around 100W per day, out of which 67W is dissipated by walking.[23] Upper body is able to output in the range of 10% of overall output which is 10W/day, this is including: exhalation(0.50W), blood pressure (0.47W), breathing band (1.0W), arm movement(75mW/arm), body heat (6.5W) [24].

Table 1- 6 Human heat emission in different activities

	total (W)	sensible (W)	latent(W)
Seated at rest	100	60	40
Seated light work	120	65	55
Seated eating	170	75	95
Walking @ 3mph	305	100	205
Heavy Work	465	165	300
Athletics	525	185	340

Source: 1977 fundamentals, ASHRE Handbook & Product Directory ambient temp= $25^{O}C$

Table 1- 7 Summary of total measured work done at each of 3 energy generating locations the E-jacket during the walking cycle

	Work[J]	Power[W]	Max torque[Nm]	Negative work %	Negative work J
Center of mass	11.3	22			
Elbow	1.1	2.6	2	39	0.8
Shoulder	1.8	3.1	2	61	1.4

(*) All the calculations are performed on 83-Kg person, assuming walking frequency of 1Hz per cycle (two steps).

(**) Center of mass includes also negative work but the magnitude is not known

CHAPTER 2
ENERGY HARVESTING SOURCES

2.0 INTRODUCTION

A variety of energy sources are utilized in a design of E-Jacket. Those are: vibration, heat and sunlight. Each of these sources differ in the amount of energy that they can produce per unit of time, type of transducer that needs to be applied and type of electrical current that can be extracted from them: DC or AC. In this study, the DC sources are thermal generator and PV cell, the AC source is piezoelectric transducer. The transducer that converts the ambient energy into electrical energy is modeled by the Thevenin's equivalent circuit as shown in Fig. 2-1. [25]

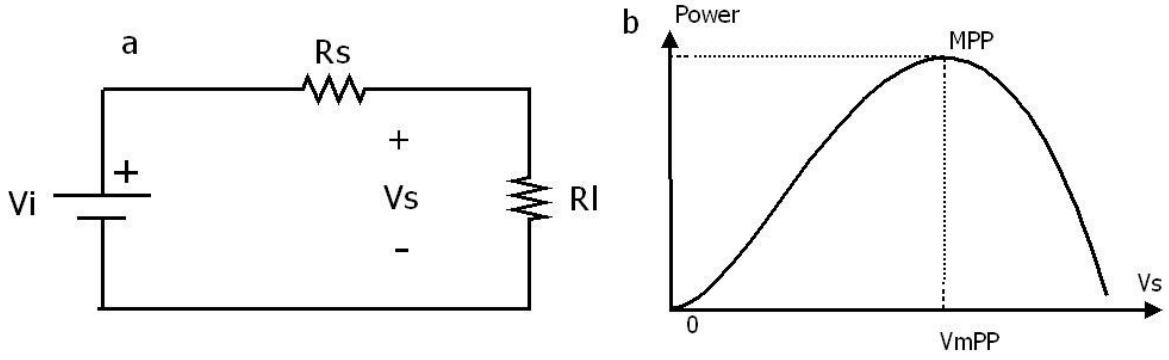

Fig.2- 1 Thevenin's equivalent circuit model for energy transducer

V_I is the Thevenin equivalent ideal voltage source and R_S is the Thevenin equivalent input resistance (Fig 2.0). These two parameters are both function of the type and size of harvester and the amount of ambient energy. In order for the source to transfer the maximum amount of energy to the load resistance R_L, the load resistance must be matched to the source resistance: $R_L = R_S$. In that case the optimal voltage across R_L is V_S, and the formula is presented in Eq.2-1.

$$Vs=\frac{V_I}{2}=V_{MPP} \quad (2\text{-}1)$$

$$\frac{V_{MPP}^2}{R_L}=\frac{V_I^2}{4R_S} \quad (2\text{-}2)$$

MPP stands for maximum power point and the maximum power is given by equation (2-2). If the voltage, V_s is not equal to V_{MPP}, than the output power will be lower than the MPP (Fig. 2-0b). If for any reason the ambient conditions change, the Power vs. Voltage curve will shift (Fig. 2.0b). This will result in loss of equilibrium and the overall system will not operate at MPP anymore and the energy transfer will not be at the maximum [26]. In energy harvester design the goal is to achieve efficient power transfer between the transducer and the energy storage device. Connecting the transducer directly to energy storage device, will result in slow and very inefficient. This problem can be addressed through maximum power point tracking (MPPT). Essentially MPPT is way of adaptively controlling the voltage regulator in order to keep the Vs as close to equal to V_{MPP}. The design methodology of the voltage regulator will depend on the type of harvester used. This will be discussed in more detailed in the following chapters.

2.1 PIEZOELECTRIC ENERGY HARVESTER

Piezo- electric energy harvesters utilize the characteristics of piezo -electric material to generate electric potential across the surface of the crystal, upon which the mechanical force is applied [27]. The potential is produced by the displacement of charges. This effect is reversible which means, that if the potential difference is applied across the piezo crystal, the shape of the crystal will be altered. This effect is known as piezoelectric effect. The materials that exhibit piezoelectric properties can be divided into two groups: (i) Natural

group and (ii) Synthetic group. Natural group materials are: quartz and rochelle alts. Synthetic group are: lithium sulphate, dipotasium tartarate, ethylene diamine tartarate and potassium dihydrogen phosphate. The piezoelectric effect can be utilized to respond to a range of mechanical deformations such as: thickness expansion, transverse expansion, thickness shear and face shear [29]. The mode of motion affected depends on the shape of the body relative to the crystal axis and location of the electrodes. Piezo electric element used for converting mechanical motion to electrical signals may be thought as charge generator and a capacitor. Mechanical deformation generates a charge and this charge appears as a voltage across the electrodes [30]. The voltage is given by equation Eq.1-1.

$$E = Q/C. \tag{2-3}$$

The pizeo electric effect is direction sensitive. A tensile force produces voltage of one polarity while a compressive force produces a voltage of opposite polarity. The magnitude and polarity of the induced charges are proportional to the magnitude and the direction of the applied force F.

$$Q = dxF \tag{2-4}$$

d= charge sensitivity of the crystal; C/N: (it is a constant for a given crystal)

F= applied force N.

The force F caused a charge in thickness of the crystal

$$F = \frac{AE}{t}\Delta t \tag{2-5}$$

Where: A= area of crystal [m^2

t= thickness of crystal [m]

E= Young's modulus, [N/m^2] = (stress/strain) is given by Eq. 2-6.

$$\frac{F}{A}\left(\frac{1}{\frac{\Delta t}{t}}\right)=\frac{Ft}{A\Delta t}\ N/m^2 \qquad (2\text{-}6)$$

From Eq. 3 and 4: the charge is:

$$Q=dAE\left(\frac{\Delta t}{t}\right) \qquad (2\text{-}7)$$

The charge at the electrodes gives rise to an output voltage:

$$E_0 = Q/C_p \qquad (2\text{-}8)$$

C_p= capacitance between electrodes:

$$C_p = \varepsilon_r\varepsilon_0 A/t \qquad (2\text{-}9)$$

$$E_0=Q/C_p=\frac{dF}{\in_r\in_0 A/t}=\frac{dt}{\in_r\in_0}\frac{F}{A} \qquad (2\text{-}10)$$

Pressure or stress:

$$P=\frac{F}{A}\ N/m^2 \qquad (2\text{-}11)$$

$$E_0=\frac{d}{\in_r}\frac{1}{\in_0}t\ P= g\ t\ P \qquad (2\text{-}12)$$

where: g = $d/\varepsilon_r\varepsilon_0$

'g' is a voltage sensitivity of the crystal. This is a constant for a given crystal cut. Its units are Vm/N

$$g=\frac{E}{t\,P}=\frac{E_{0/t}}{P} \tag{2-13}$$

Now E_0/t is the electric filed intensity in the crystal and P is the pressure or the applied stress to the crystal. Therefore, crystal voltage sensitivity, g, can be defined as the ratio of the electric filed intensity to pressure (or stress). Now $E_0/t = \varepsilon$ is the electric fielded intensity in the crystal and P is the pressure or the stress applied to the crystal. Therefore, crystal voltage sensitivity, g, can be defined as the ratio of the electric filed intensity to pressure. The units of 'g' are Vm/N.

From equation Eq. 10, charge density:

$$d= \varepsilon_r\varepsilon_0\, g \quad C/N \tag{2-14}$$

Piezoelectric transducers can be modeled using the electric circuit in Fig. 2-2.

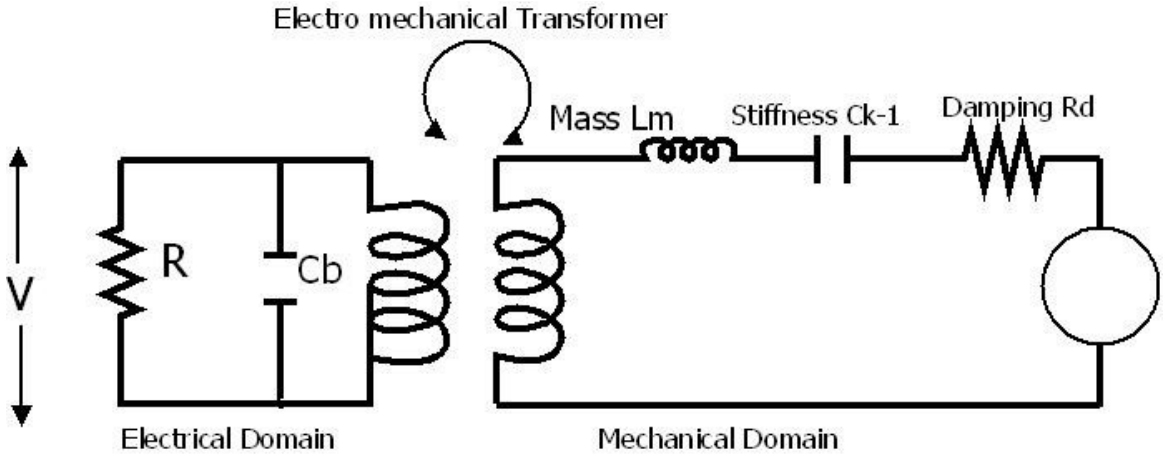

Fig.2- 2 Electrical circuit equivalent of piezoelectric harvester

Equivalent circuit model of a piezoelectric single degree of freedom resonating system consist of Electrical Domain and Mechanical domain [31]. Mechanical domain's parameters are: Force (F), velocity(v), mass(m), compliance(K^{-1}), damping(D). Electrical equivalent parameters are presented in Table 2-1.

Table 2- 1 Mechanical parameters and equivalent electrical parameters

Electrical Equivalent	Mechanical Parameter
Voltage(V)	Force(F)
Current(i)	Velocity(v)
Inductance (L)	Mass(m)
Capacitance (C)	Compliance(K^{-1})
Resistance (R)	Damping

Electromechanical coupling coefficient, k, determines ability of material to convert input mechanical vibration to usable electrical output. The higher the **k** the better the ability of the material to convert mechanical strain to electrical field. Material piezoelectrical element based on PZT-5H was chosen due to its superior conversion characteristics, and is available in suficinetly thick structutre to be robust.(Table 2-2)

Table 2- 2 Different Piezoelectric material and their K values

Material[1]	**K33**	**K31**
$Pb(Zr_x Ti_{x-1})O_3$ (PZT-5H)	0.75	0.39
$Pb(Zr_x Ti_{x-1})O_3$ (PZT-5A)	0.71	0.31
$BaTiO_3$	0.48	0.21
PVDF	0.15	0.12

2.1.1 PIEZOELECTRIC SCAVENGER DESIGN

During the design of the piezoelectric scavenger, it is important to take into an accent the following equation for maximum power output:

$$P \propto \frac{a_{in}^2}{\omega} m \qquad (2\text{-}15)$$

Power is proportional to scavenge peaks with maximum accelerations (a) squared (identified as accelerations associated with walking), the design should operate at lowest possible available resonant frequencies (ω) (lowest resonance frequency associated with walking is 2Hz). Measured power efficiency of the piezeo harvester is given in Fig. 2-3.

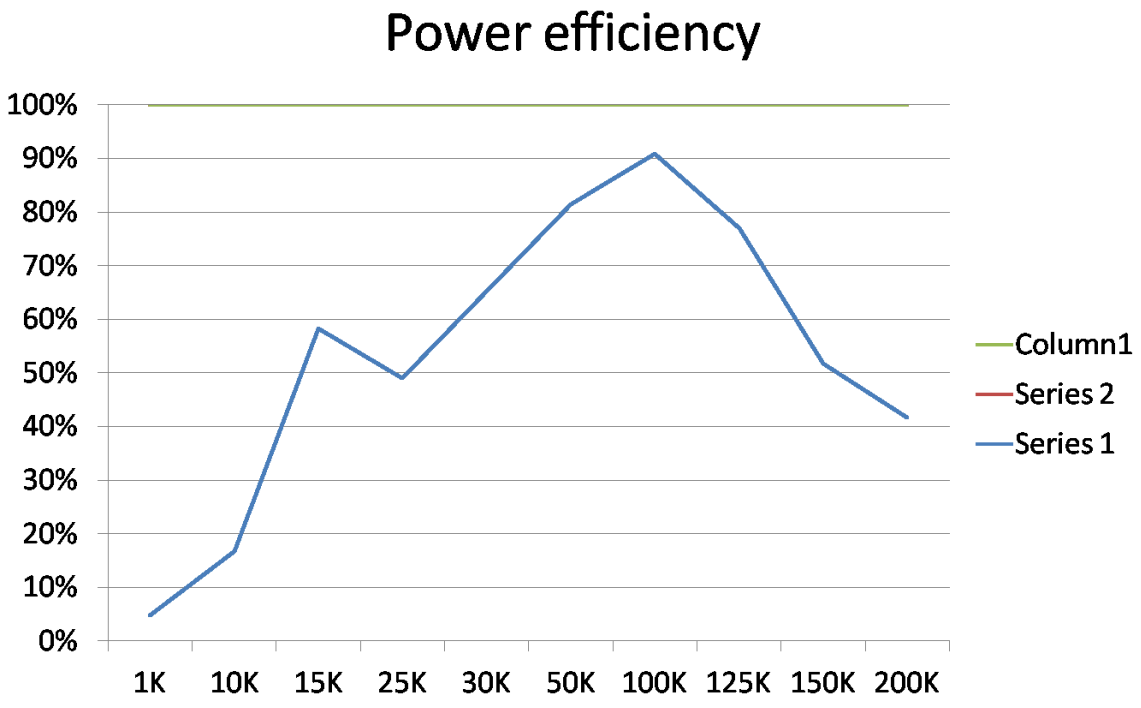

Fig.2- 3 Power Efficiency of the piezo harvester used in E-jacket

Overall mass is very important [33]. It is desirable to be as heavy as possible (m); however, the heavier the device the larger the mechanical damping therefore there will be a trade off in efficiency as device weight is increased. Table 2-2 offers theoretical power output based on input frequency of 0.2 mg.

Table 2- 3 Theoretical power output based on input frequency of 0.2 mg

Operating Frequency (Hz)	Power (mW)
2	100
4	63
6	20

2.2 HARVESTING OF THE VABRATION ENERGY

A fairly narrow frequency band must be selected from which to scavenge energy [34]. Different modes of motion or transportation produce different vibrations, for example walking is relatively low frequency and running is higher. Damping of the vibrations can significantly reduce the energy available to scavenging. Data was obtained with the intention that a device to scavenge these vibrations would be mounted rigidly to the E-jacket itself. The subject was running and the following acceleration data was obtained (Fig 2-4).

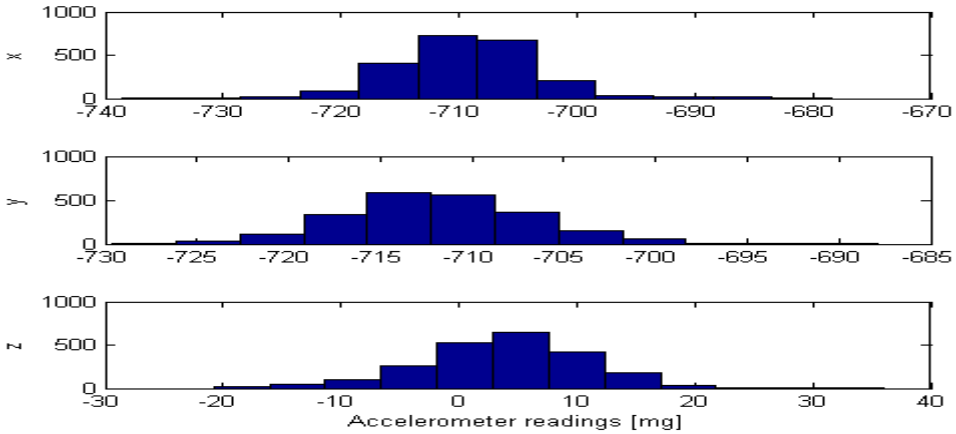

Fig.2- 4 Acceleration data obtained for running at 10Hz

The piezoelectric material used for thus study is PZT-5H due to its superior conversion characteristics, and is avelable in suficinetly thick structutre to be robust. Table 2-4 contains the basic material parametric data.

Table 2- 4 Piezoelectric material properties

Value	Parameter
d_{31} (m/V)	$-310x10^{-12}$
d_{33}(m/V)	$590x10^{-12}$
r(kg/m^3)	7600
Q	32
$E_{3(}$GPa)	50
E_1(Gpa)	60
Θ_{33}(@1KHz)	3800
E_p(V/m)	$2X10^6$
E_c(V/m)	$8.3x\ 10^5$

2.3 THERMAL ENERGY HARVESTER

Temperature gradients and heat flow are present in natural and human-made environments and offer the opportunity for energy harvesting. Certain semiconductor materials have an inherent physical property to generate electrical current as a response to external stimuli [35].

2.3.1 SEMICONDUCTOR PHYSICS FOR TEGs

Thermoelectric generators are solid-state devices with no moving parts. They are silent, reliable, and scalable, making them ideal for small, distributed power generation, and energy harvesting [36]. The thermoelectric effects arise because charge carriers in metals and semiconductors are free to move much like gas molecules while carrying charge as well as heat. When a temperature gradient is applied to a material, the mobile charge carriers at the hot end preferentially diffuse to the cold end [38]. The buildup of charge carriers results in a net charge (negative for electrons, e− and positive for holes, h+) at the cold end, producing an electrostatic potential (voltage). Equilibrium is thus reached between the chemical potential for diffusion and the electrostatic repulsion due to the buildup of charge.

2.3.2 SEEBECK EFFECT

The Seebeck effect describes the generation of an electrical voltage due to a temperature difference between a weld of two different materials and the other side of these two wires. This is illustrated in figure bellow (Fig. 2-3)

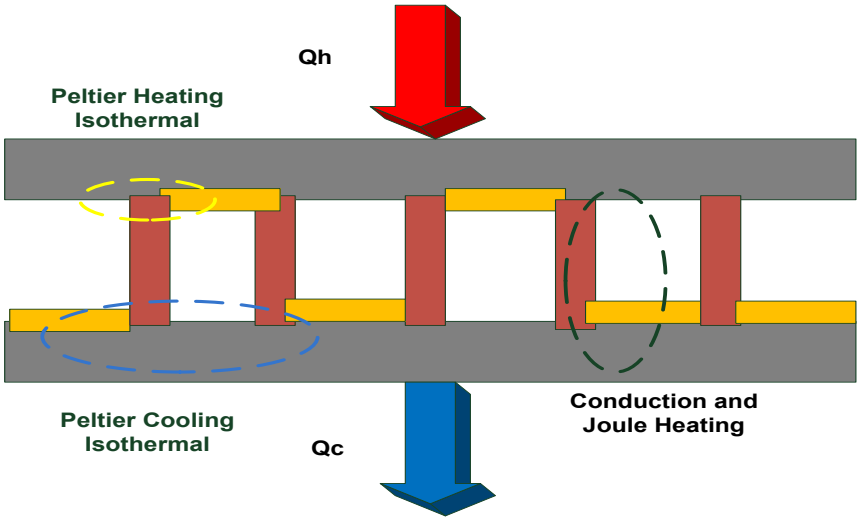

Fig.2- 5 Thermoelectric Effect

A voltage difference is only measured when T1≠T2. The Seebeck effect can be described by

$$\Delta V = \alpha_s \Delta T \qquad (2.16)$$

Where:

- ΔV (V) is the generated voltage difference,
- α_s (μV K-1) the Seebeck coefficient
- ΔT (K) the absolute temperature difference.

Carnot

$$\acute{\eta} = \frac{T_H - T_C}{T_H}\left[\frac{\sqrt{1+ZT_m}-1}{\sqrt{1+ZT_m}+\frac{T_C}{T_H}}\right] \qquad (2\text{-}17)$$

$$ZT = \frac{\alpha^2}{pk}T = \frac{\sigma\alpha^2}{k}T \qquad (2\text{-}18)$$

Where:

- α^2 is a Seabeck effect

- p is electrical resistivity
- k is a thermal conductivity
- σ is electrical conductivity

Good thermoelectric materials have:

- High Seebeck coefficient (V/K)
- Low electrical resistivity (Ω-m)
- Low thermal conductivity (W/mK)

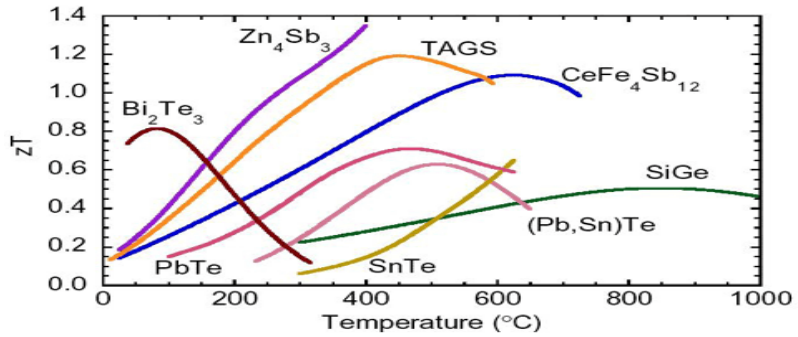

Fig.2- 6 Relationship between ZT and Temperature for various materials

Industry standard materials have ZT that range from 0.6 to 1.2, but you can find published results for materials with higher ZT. A plot of various p-type semiconductor figures of merit times temperature vs. temperature are shown. Within the temperature ranges concerned in electronics cooling (0-200C^0) Bi_2Te_3 performs the best (Fig. 2-6). E-Jacket application is utilizing the properties of Thermo-electrical generators to harvest the energy from human body. This application is particularly well suited for the cold environments. In fact as the outside temperature is decreasing, more harvested energy will be available for powering the electronics of the E-Jacket. The principle is best illustrated in Fig. 2-7.

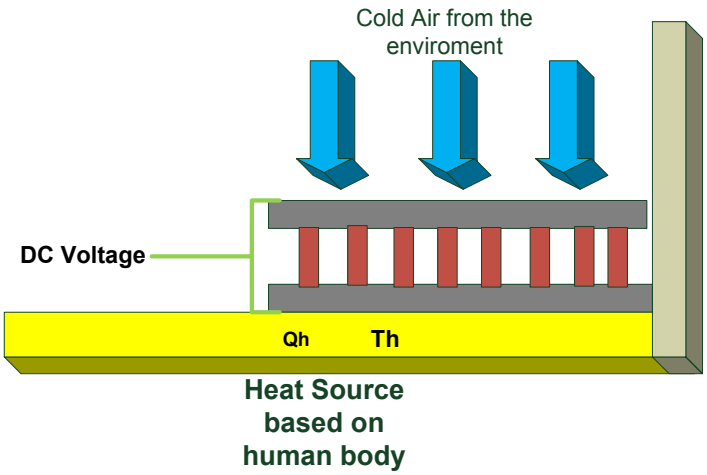

Fig.2- 7 Principle of thermal energy harvesting in E-Jacket application

TEG elements are very affordable, however their drawback is very small output voltage that can range anywhere from 5mV-200mV. Special consideration needs to be taken into an account when designing electrical systems for power conversion. The simple and inexpensive TEG element is used for E-jacket applications shown below in Fig. 2-8.

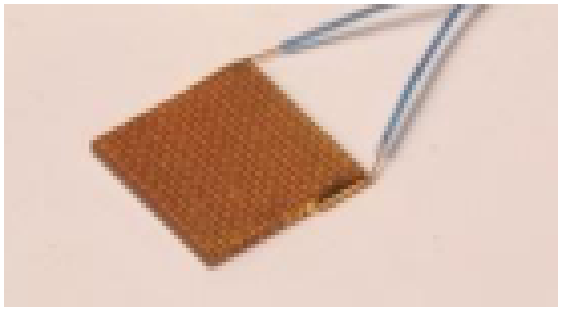

Fig.2- 8 Energy Harvesting TEG from Heat Sink Inc.

2.3.3 DESIGN OF TEG HARVESTER

When designing a TEG system, it is important to consider EH design equation to solve for the best number of couples and element length to area ratio:

Table 2- 5 Electrical and thermal consideration for the TEG system

Electrical Considerations	**Thermal considerations**
Electrical resistance of TEG is a function of element dimensions and electrical resistivity	Thermal resistance of TEG is a function of element dimensions and thermal conductivity
$R_{TEG/elc}=N\frac{L}{A}(\varrho_p-\varrho_n)$	$R_{TEG,th}=\frac{L}{NA(K_p-K_n}$
Electrical load resistance ratio: $n=\frac{R_L}{R_{TEG}}$	Thermal load resistance ratio: $m_r=\frac{R_{TG,th}}{HSR+CSR}$

Thermal and electrical matching is presented in Eq.(2-19)

$$n=\frac{R_L}{R_{TEG}}=1 \quad m=\frac{R_{TG,th}}{HSR+CSR}=1 \tag{2-19}$$

Fig.2- 9 Thermal and Electrical equilibrium of the system

Human body emits heat; therefore heat can be harvested from human body.

Multiple heat harvesting systems are placed in different locations on the E-Jacket including: chest area, under the arm, closer to the mouth and on the hood of the jacket. These areas have been identified as highest blood circulation areas, which mean that heat released around those

areas will be highest. Carnot efficiency puts an upper limit on the heat energy that can be recovered. The temperature difference between the human body and the outside environment can be harvested. Carnot efficiency with this temperature conditions is in the range of 8%. In a warmer environment the Carnot efficiency drops while in a colder environment the Carnot efficiency rises. The recoverable energy yields 3.1-6.2 W of power. However, evaporative heat loss account for 25% of the total heat dissipation, and therefore the maximum power available drops to 2.5-4.1 W.

2.4 SOLAR ENERGY

Solar energy is created at the core of the sun when hydrogen atoms are fused to form helium by nuclear fusion. It is estimated that 700 million tons of hydrogen are converted into 695 million tons of helium every second.

$$\mathbf{H^{+} + H^{+} = He^{++} + Energy}. \qquad (2\text{-}20)$$

The remaining mass of 5 million ton is converted into electromagnetic energy that radiates from the sun's surface out into space. The rate at which energy is emitted from the sun's surface is estimated at 63,000,000 W/m^2. However the earth intercepts only a small fraction of this enormous energy. When travelling through outer space, which is characterized by vacuum, the solar radiation remains intact and is not modified or attenuated until it reaches the top of the earth's atmosphere [39]. The energy emitted from the sun and intercepted by the earth is estimated at a rate of 1.73 x 10^{14} kW. It is largely comprised of the following approximate ratios. Fig 2-8 illustrates spectral radius of sun's energy.

– 9% ultraviolet radiation (100 – 400 nm)

– 41% visible radiation (400 – 700 nm)

– 50% infrared radiation (700 – 3000 nm)

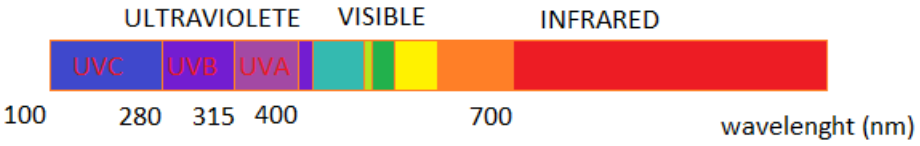

Fig.2- 10 Energy Spectrum emitted from the Sun

The amount of power received at the top of the earth's atmosphere is estimated at 1.368 kW per m^2. This is called the ***solar constant***. On average 30% of this energy is reflected back into space. While travelling towards the earth's surface another 20% is absorbed in the atmosphere. A number of atmospheric gases namely, ozone (O_3), oxygen (O_2) carbon dioxide (CO_2), water vapor (H_2O), nitrous oxide (N_2O), carbon monoxide (CO) and methane (CH_4) have been identified as having observable absorption features in the 200 –2500 nano-meter wavelength range. Fig. 2-10 illustrates by spectrum analysis the effects of absorption at various wavelengths. Approximately 50% of the original radiation (from the Sun) passes through to the earth's surface.

2.4. 1 SOLAR POWER COLLECTION

Energy output of the solar collector will depend on the global radiation available per unit area as well as the size of the solar collector. Global radiation is the total amount of radiation arriving at a location. It is comprised of **direct and diffuse** components. There are two variables that affect amount of INSOLATION (incident solar radiation) at an earthly location namely

(i) **Geometric factors:** (altitude, latitude), orientation, season, and climate

(ii) **Atmospheric factors**. gasses, air mass and perspiration

2.4.2 INSOLATION

Insolation I is the amount of radiation per unit area over a given season. It has to be maximized in order to minimize the size and therefore the cost of the solar energy collector. Low values of **insolation** mean that larger and therefore more expensive surfaces must be used to collect the same amount of solar energy. **Maximum radiation** per surface is obtained when the collector surface is positioned perpendicular to sun's rays. A collector must be able to track the sun throughout the day and over the seasons to maximize energy capture [40]. This can be achieved by mounting the panel on a sun-tracking device. In most practical situations however, this may not be possible for various reasons including economics. In such cases a panel can be positioned at a mean (or compromise) inclination in order to optimise energy capture as depicted in Fig. 2-11.

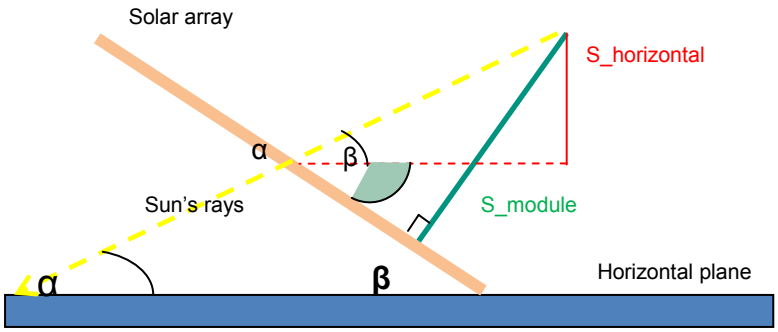

Fig.2- 11 Solar panel inclination angles for optimum energy absorption

From a geometrical point of (clear sky) insolation is given by

$$\mathbf{I = S \cos \theta_Z} \qquad \textbf{(2-21)}$$

Where S (ONE SUN) = 1000 W/m^2 – is a theoretical value of solar insolation for a clear day on a surface perpendicular to incoming sun's rays**. θ_Z is called the zenith angle**, which is basically the angle by which the position of the sun deviates from the observer's overhead

position. The value of θ_Z is determined by three factors: location (latitude), time of the day (hour) and season of the year (declination). The respective angles are Φ (the latitude angle), H (the hour angle) and δ (the angle of declination). θ_Z, which is given by the following expression.

$$\theta_Z = \cos^{-1} (\sin\Phi \sin\delta + \cos\Phi \cos\delta \cos H) \quad \textbf{(2-22)}$$

Declination δ is the angle of deviation of the sun from directly above the equator.

$$\delta = 23.45° \sin \frac{\left(360(n-80)\right)}{365} \quad \textbf{(2-23)}$$

The numbers of daylight hours:

$$DH = \frac{48}{360} \times \cos^{-1}\left(-\tan\phi \tan\delta\right) \quad \textbf{(2-24)}$$

The optimal performance for a flat array (non-tracking) occurs if the angle to the horizontal is $\phi - \delta$. The panel can also be set to capture the most energy over a season.

2.4.3 PHOTOVOLTAIC SOLAR PANELS

As inferred from the name, **photovoltaic**, which is a combination of the Greek word " ***Photo*** " which means light and " ***Voltaic*** " which means electric, the fuel needed for this generating system is sunlight. In a nutshell, photovoltaic means light to electricity. Becquerel first reported the **photovoltaic effect** in 1839. Bell Laboratories produced the first practical silicon type solar cells in 1954. Initial applications were in extraterrestrial missions.

The solar panels are mainly made out of semiconductor material, Silicon being the most abundantly used semiconductor. When the energy from sunlight, known as photons, strikes the electrons in the semiconductor, some of these electrons will acquire enough energy to leave the valence band and enter the conduction band. When this occurs, the electrons in the conduction band begin to move creating electricity. As soon as the electron leaves the valence band, a positively charged hole will remain in the location the electron departed.

2.4.4 EFFICINECY OF SOLAR PANNELS

Solar power would be the leading source of energy if it there was a way to efficiently extract a majority of the energy delivered to the earth from the sun on a daily basis. On the equator at noon, 1000 watts/m^2 of sun energy touches the ground. Unfortunately only up to 20 percent of this power can be transferred into usable energy. This inefficiency is directly related to the percentage of photons that are absorbed. The electrons in the semiconductor material will only jump into the conduction band if they absorb a photon. The photons can either be absorbed, reflected, or can even pass right through the semiconductor. A solar panel's output varies depending on certain ambient weather conditions such as: ***temperature, illumination, how clear the sky is*** and so on. These aspects need to be taken into account when designing the maximum amount of power from the solar panels, regardless of how efficient or inefficient the solar panels may be.

2.4.5 VOLTAGE-CURRENT (V-I) CHARACTERISTICS

PV cell is a dc generator. When an external electrical load is connected, a dc current (called the photo current) flows.

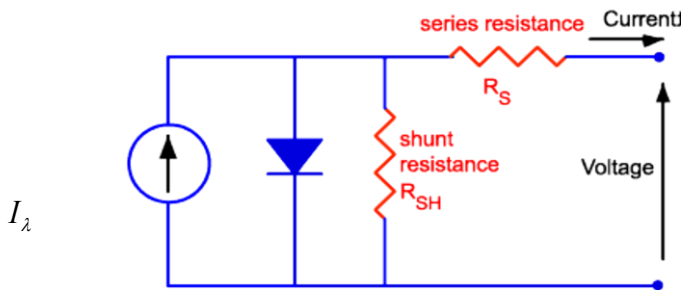

Fig.2- 12 Equivalent Circuit representation of PV panel

Fig. 2-12 shows the equivalent circuit of a solar cell. I_λ is the current generated by the cell as a result of the light radiating on the cell. I_d is the reverse saturation current of the diode, typically 100 pA for the silicon cell. I*p* represents the leakage current to the ground. R*p* is used to set the correct value of I*p*. R*s* is a series resistance, it depends on impurities (dopants), size of junction. I*o* is the output current to the load.

$$I_o = I_\lambda - I_d - I_p$$
$$where \quad I_d = I_s\left(e^{\frac{qV_d}{KT}} - 1\right) \qquad (2\text{-}25)$$

q is the electron charge ($1.6\text{x}10^{-19}$ coulombs)

V_d is the diode voltage

K is the Boltzman constant $1.38 \text{ x } 10^{23}\ J$

***T* is the temperature in Kelvin**

Therefore

$$I_o = I_\lambda - I_d - \frac{V_d}{R_p} \qquad (2\text{-}26)$$

For a load resistance R_L connected to the output of the cell,

$$I_o = \frac{R_p}{R_p + R_s + R_L}\left[I_\lambda - I_s\left(e^{\frac{qV_d}{KT}} - 1 \right) \right] \tag{2-27}$$

Therefore output power

$$P_o = V_d I_o = \frac{V_d R_p}{R_p + R_s + R_L}\left[I_\lambda - I_s\left(e^{\frac{qV_d}{KT}} - 1 \right) \right] \tag{2-28}$$

Extracting the maximum amount of power from the solar panel is difficult due to the nonlinearity of the Voltage-Current (V-I) characteristic. Figure 2-13 shows the V-I characteristics.

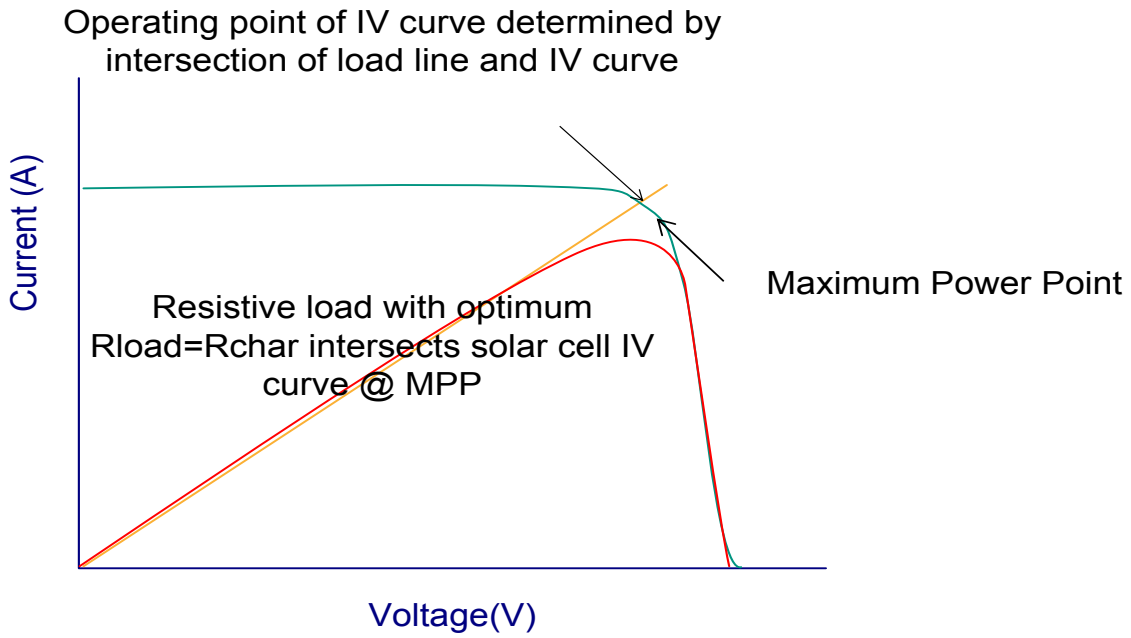

Fig.2- 13 Voltage-Current-Power Characteristics of PV panel

To get the maximum power from the solar panel, the solar panel must always be operated at or very near the point where the power curve is at a maximum, its peak point. However, this

operating point will constantly change due to the constantly changing ambient conditions. In fact, the temperature and other affects such as irradiance alter the V-I characteristic changing the operating point that would allow us to pull out the maximum amount of power. As a result, we need to constantly track the power curve and keep the solar panel operating at the point where the maximum amount of power would be achieved. Irradiance value is altered significantly depending on geographical location, the angle of the sun, and the amount of haze or cloud cover preventing all of the suns energy from reaching the ground. Since solar panels run strictly off the energy emitted from the sun, their output is affected by the changing irradiance.

CHAPTER 3
HUMAN BODY MONITORING IN OUTDOOR ENVIROMENT

3.1 INTRODUCTION

Monitoring human body motion has been of great interest to people of various disciplines over the past few years. Research has been directed towards applications in healthcare, entertainment, and education **Error! Reference source not found.**. Body area sensor networks (BASN) and wireless sensor networks (WSN) provide non-invasive methods to track the physical behavior of people while using low-power radios to receive and transmit data. Barth et al. 0 have proposed a body area sensor platform called "TEMPO" (Technology Enabled Medical Precision Observation) that measures linear acceleration and rate of rotation about three axes. "TEMPO" is used by many research groups, but one of the shortcomings is that all collected data needs to be transferred wirelessly to a host machine in order to be stored. This can be a limiting factor when the head motion tracking device is to be worn throughout the day while engaging in day-to-day activities. Wearable sensor modules can be used for *gait analysis*, and Chen et al. 0 have proposed a gait evaluation system called "LEGSys" (Locomotion Evaluation and Gait system), which uses 9-degree-of-freedom inertial sensors to analyze leg movement. The advantage of this system is that it allows gait analysis experiments to be conducted outside of laboratory environments in order to capture natural gait patterns. Najafi et al. 0 have used the LEGSys device to provide experimental results and to analyze the reliability of the system. The accelerometers used in the LEGSys system have a maximum range of +/- 2g, and more notably, the weight of the system is nearly 200g where the sensor, the data unit, and the battery weigh 10g, 80g, and 104g respectively. While

such weight is not a concern for a device that is worn on legs, the weight is one of the major design constraints when the device is to be worn on a person's head.

Another aspect of gait analysis is estimating walking speed. Vathsanam et al. have proposed such speed estimation by using a Gaussian Process-based Regression (GPR) technique and have compared the performance with Bayesian Linear Regression (BLR) and Least Squares Regression (LSR) 0. The limitation here is that experiments were performed in a laboratory, so the resemblance to natural behavior has been removed from the results they have presented. Neural network based speed estimation from tri-axial accelerometer data has been proposed by Yoonseon et al. where they use an accelerometer with a range of +/- 3g 0. Although the sensor module is only 23g, there is an additional data collection device that must be worn on a belt as well. S. Chen et al. have proposed a TEMPO based gait analysis technique. Activity recognition is another common application of wearable sensors. Ravi et al. **Error! Reference source not found.** have analyzed several classification methods for accelerometer based activity recognition, and some of these include decision trees, decision tables, k-nearest neighbors, and naïve Bayes. Suutala et al. have presented a daily activity recognition system based on support vector machines (SVM) **Error! Reference source not found.**.

3.2 CALIBRATION AND SIGNAL PROCESSING

The objective of this section is to present the theoretical background used for sensor integration. First, the least square method used to calibrate the sensors is described. Then, basic theory behind the implementation of finite impulse response (FIR) filters and Kalman filters is discussed. FIR filters are required to filter out the high frequency noise of accelerometers and magnetometers and the low frequency drifts of gyroscopes. Kalman

filters are used to fuse readings from multiple sensors in order to obtain meaningful outputs such as orientation angles and translational speeds. Next, equations used to compute orientation angles of the IMU and rotation matrices used to transform the coordinate system of IMU data are presented.

3.2.1 THE LEAST SQURE METHOD

The sensitivity of sensors can degrade over time, and usually the factory calibration varies from device to device. Therefore, it is necessary to calibrate and re-calibrate sensors periodically 0. The least square method is commonly used to estimate parameters and to fit a function to a data set using an over-determined system of equations. The optimum parameters found by the least squares method minimize the sum of residuals, which is given by,

$$S = \sum_{i=1}^{N}(y_i - x_i)^2 \tag{3-1}$$

Where y_i and x_i refer to the i^{th} value of the known fitting function and the data set respectively 0. Data points y_i and x_i can be placed in matrices, and a matrix B can be defined to contain the parameters that need to be estimated. The matrix relationship can simply be stated as:

$$Y = X \cdot B \tag{3-2}$$

The calibration parameter matrix denoted by X can be computed as

$$B = [X^T \cdot X]^{-1} \cdot X^T \cdot Y \tag{3-3}$$

Equation (3-3) can be used to determine calibration parameters for the accelerometer and the gyroscope. In the case of the accelerometer, the compensated values are related to the raw measurements as seen below **Error! Reference source not found.**:

$$\begin{bmatrix} A_{x1} \\ A_{y1} \\ A_{z1} \end{bmatrix} = \begin{bmatrix} ACC_{11} & ACC_{12} & ACC_{13} \\ ACC_{21} & ACC_{22} & ACC_{23} \\ ACC_{31} & ACC_{32} & ACC_{33} \end{bmatrix} \cdot \begin{bmatrix} A_x \\ A_y \\ A_z \end{bmatrix} + \begin{bmatrix} ACC_{10} \\ ACC_{20} \\ ACC_{30} \end{bmatrix} \tag{3-4}$$

$A_{x1,}$ $A_{y1,}$ and A_{z1} are the known acceleration values while $A_{x,}$ $A_{y,}$ and A_z are the raw measurements and ACC_{x0} are the bias values. The entries on the diagonal (ACC_{11}, ACC_{22}, ACC_{33}) are the gain values of each of the axes, and the off diagonal entries refer to the amount of crosstalk between axes. As suggested in **Error! Reference source not found.**, the above relationship can be rearranged to be more suitable for least square computation as follows:

$$[A_{x1} \quad A_{y1} \quad A_{z1}] = [\,A_x \quad A_y \quad A_z \quad 1] \cdot \begin{bmatrix} ACC_{11} & ACC_{21} & ACC_{31} \\ ACC_{12} & ACC_{22} & ACC_{32} \\ ACC_{13} & ACC_{23} & ACC_{33} \\ ACC_{10} & ACC_{20} & ACC_{30} \end{bmatrix} \quad (3\text{-}5)$$

The relationship described by eq. (3-5) can also be used to calibrate the gyroscope and the magnetometer on the.

3.2.2 FIR FILLTER

The accelerometer and the gyroscope are micro electro-mechanical systems (MEMS) based devices. Often, sensor readouts are corrupted by noise inherent to MEMS processes, as well as by noise caused by external influences such as mechanical vibrations. In order to ensure the reliability of recorded data, it becomes necessary to filter out the high frequency noise of accelerometers and magnetometers and the low frequency drifts of gyroscopes. These filters need to be stable and have linear phase. Therefore, finite impulse response (FIR) filters based on the Kaiser Windowing technique are to be implemented 0.

The order of the FIR filter can be approximated by Eq. (3-6),

$$M \approx (A - 7.95)/(14.36\,\Delta f) \quad (3\text{-}6)$$

Where A refers to the maximum sideband ripple and Δf is the normalized transition band defined by,

$$\Delta f = (f_c - f_r)/(f_s/2) \tag{3-7}$$

f_c ,f_r, and f_s refer to cutoff, first stop band, and sampling frequency respectively. The parameter β used to define the shape of the Kaiser window is defined as:

$$\beta = 0.1102(A - 8.7) \tag{3-8}$$

3.3 SENSOR FUSION

In order to obtain the correct orientation at any given point, it is necessary to effectively fuse the measurements of the accelerometer, gyroscope, and the magnetometer.

3.3.1 COMPLEMENTARY FILTER

A complimentary filter combines the angle estimates obtained using accelerometers and integrating gyroscope readings by weighing them based on the dynamics of the system. Accelerometer based angles are filtered using a low pass filter, and gyroscope based angles are filtered using a high pass filter before summing the two angle estimates. The structure of the complimentary filter is illustrated in Figure 3-1.

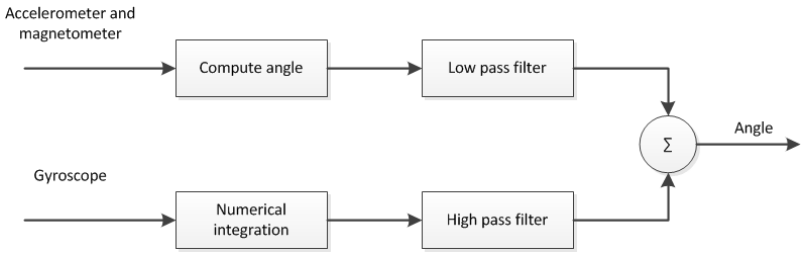

Fig. 3- 1 The structure of the complimentary filter

3.3.2 KALMAN FILTER

A standard Kalman filter estimates the states of a discrete-time process described by the following equations:

$$x_{k+1} = A_k x_k + B_k u_k + w_k \tag{3-9}$$

$$y_k = H_k x_k + v_k \tag{3-10}$$

Where,

- A, B, and H are state transition, input, and output matrices respectively
- x_k and y_k are the state vector and the output at the k^{th} time step respectively
- u_k is the known control signal (input)
- w is the process noise with covariance matrix Q
- v is the measurement noise with covariance matrix R

The Kalman algorithm is described in Figure 3-2.

Predict – time update
1. Project the state ahead $\hat{x}_k^- = A\hat{x}_{k-1} + Bu_{k-1}$ 2. Project the error covariance
$P_k^- = AP_{k-1}A^T + Q$
Correct – measurement update
1. Kalman gain $K_k = P_k^- H^T (HP_k^- H^T + R)^{-1}$ 2. Error of the estimated state $\hat{x}_k = \hat{x}_k^- + K_k(y_k - H\hat{x}_k^-)$ 3. Update the error covariance

Fig. 3- 2 The Kalman filter algorithm – adapted from [40]

The Kalman filter can be used to fuse gyroscope, accelerometer, and magnetometer measurements to estimate the orientation angles. In addition, the Kalman algorithm can be used to estimate the speeds of subjects wearing the E-jacket by fusing lateral and forward acceleration measurements as described in section **Error! Reference source not found.**.

3.3.3 TILT ANGLE COMPASATION

The E-jacket tracking device is to be used by persons of various disciplines; therefore, it is not easy to guarantee that they will always align the device perfectly with the global x, y, and z coordinates. As such device should be intelligent enough to compute the initial orientation using data from the first few seconds of measurement and adjust subsequent measurements accordingly. It is assumed that the device is stationary when the device is turned on. Therefore, the orientation angles can be estimated using the accelerometer readings as shown by the following equations **Error! Reference source not found.**. The roll and pitch angle axes are as defined in Figure 3-2.

$$Roll = \alpha = \tan^{-1}\left(\frac{A_x}{\sqrt{{A_y}^2 + {A_z}^2}}\right) \tag{3-11}$$

$$Pitch = \beta = \tan^{-1}\left(\frac{A_y}{\sqrt{{A_x}^2 + {A_z}^2}}\right) \tag{3-12}$$

The heading angle, defined as the rotation from the magnetic north, cannot be computed using only accelerometer data, and therefore, magnetometer data are also used **Error! Reference source not found.**.

$$M_x^{'} = M_x cos(\alpha) - M_y sin(\beta) sin(\alpha) + M_z cos(\beta) sin(\alpha) \quad (3\text{-}13)$$

$$M_y^{'} = M_y cos(\beta) + M_z sin(\alpha) \quad (3\text{-}14)$$

$$\gamma = 90 - \tan^{-1}\left(\frac{M_x^{'}}{M_y^{'}}\right), when\ M_y^{'} > 0 \quad (3\text{-}15)$$

$$\gamma = 270 - \tan^{-1}\left(\frac{M_x^{'}}{M_y^{'}}\right), when\ M_y^{'} < 0 \quad (3\text{-}16)$$

The following rotation matrices can then be used to project the sensor readings onto the global coordinate system for further processing[3-17].

$$R_x(\alpha) = \begin{bmatrix} 1 & 0 & 0 \\ 0 & \cos\alpha & -\sin\alpha \\ 0 & \sin\alpha & \cos\alpha \end{bmatrix} \quad (3\text{-}17)$$

$$R_y(\beta) = \begin{bmatrix} \cos\beta & 0 & \sin\beta \\ 0 & 1 & 0 \\ -\sin\beta & 0 & \cos\beta \end{bmatrix} \quad (3\text{-}18)$$

$$R_z(\gamma) = \begin{bmatrix} \cos\gamma & -\sin\gamma & 0 \\ \sin\gamma & \cos\gamma & 0 \\ 0 & 0 & 1 \end{bmatrix} \quad (3\text{-}19)$$

3.3.4 PATERN RECOGNITION

One of the major concepts of activity recogntion is *pattern recognition*, and this process involves three major steps as seen in Figure 3-3. Pattern recognition is important in detecting "man down" situtaions, hig force impacts, collision and etc.

Fig. 3- 3 Pattern recognition process

Once data has been collected, patterns need to be observed, and distinguishing features of each of the activities need to be extracted. The simplest method to identify a given task is to use the naïve Bayes classifier. The algorithm assumes that features that make up a class are independent, which makes computation simple and effective, and the algorithm performs very well even with dependent features. The sample data set is referred to as evidence (*E*), and the probability of *E* being in class *c* is given by

$$p(c|E) = \frac{p(E|c)\cdot p(c)}{p(E)} \tag{3-20}$$

E is classified as class *c* if

$$f_b(E) = \frac{p(c|E)}{p(\bar{c}|E)} \geq 1 \tag{3-21}$$

Where $f_b(E)$ is called a Bayesian classifier and $\bar{c}$ is the complement of class *c*. The probabilities based on all features of the evidence sample can be computed as follows:

$$p(E|c) = \prod_i^n p(x_i|c) \tag{3-22}$$

Where $p(x_i|c)$ refers to the probability of each feature given the class. The probability desnity function for normal distribution can be used to compute each of the total probabilities in a matrix sense as follows.

$$p(X) = \frac{1}{(2\pi)^{n/2}\sqrt{\det(\Sigma)}} \cdot e^{-\frac{1}{2}(X-\mu_x)^T \Sigma^{-1}(X-\mu_x)} \tag{3-23}$$

Where,

- μ_x is the mean vector of the features
- Σ is the variance-covariance matrix
- n is the number of elements in the feature vector

3.3.5 OTHER PATERN RECOGNITION MODELS

Several other pattern recognition algorithms are found in literature. Some of them include: support vector machines (SVM), logistic regression, k-means, and k-nearest neighbors. The SVM algorithm allows non-probabilistic classification, but one of the short-comings is that training has to be supervised. Since one of the long-term objectives of the design is to autonomously identify the motion of different users, it is necessary to use an algorithm that supports unsupervised motion. Logistic regression uses an iterative method to determine the maximum likelihood of regression coefficients, which results in a lack of convergence in some cases. The k-means algorithm is initialized by randomly assigning input data into '*k*' classes. The means of each class are first computed. Next, each data sample is assigned to the class with the nearest mean. The disadvantage of this method is that different initial classes can result in different final classes, and the process needs to be repeated to ensure reliable classification. Therefore, the Bayesian classfication method along with the expectation maximization algorithm due to their simple, yet accurate implementation.

The preceding figure suggests that accelerometer readings exhibit a near Gaussian distribution. The mean values of the readings are tabulated below:

Table 3- 1 Mean values of acceleration data in mg

Axis	**X**	**Y**	**Z**
Pre-calibration	-722.9606	-720.5112	-13.0563
Post-calibration	-709.5025	-711.8439	3.8047
Error (%)	0.39	0.69	n/a

It is evident that the least square calibration method gives parameters that result in accelerometer readings that are within less than 1% of the expected mean values. The computed calibration parameters were included in the firmware, so the end user does not have to recalibrate the device prior to using it .A turntable that can provide oscillations up to

10Hz with a maximum angular rate of 100dps was used to calibrate the three-axis gyroscope. The turntable was oscillated at 1Hz, 2Hz, and 10Hz with amplitudes of 38dps, 35dps, and 90dps respectively. The experiment was repeated for both the y-axis and the z-axis in order to generate the required matrices for the least square parameter estimation problem. Figure 3-4 demonstrates the measured data.

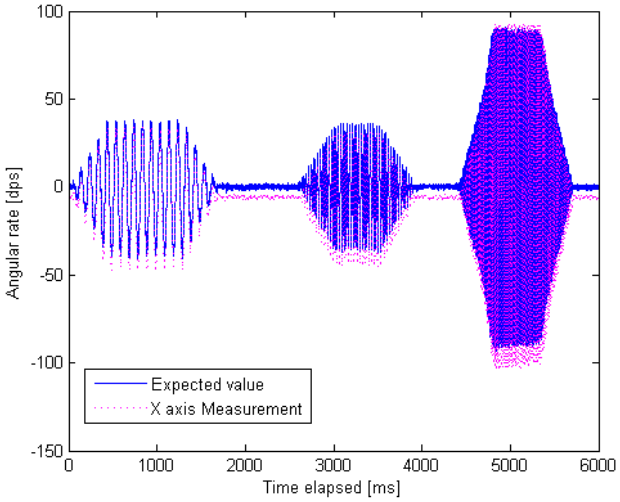

Fig. 3- 4 Comparison of the expected gyroscope readings and the measurements values about the x-axis

The computed set of gyroscope calibration parameters is as follows:

$$\begin{bmatrix} Gyro_{11} & Gyro_{12} & Gyro_{13} \\ Gyro_{21} & Gyro_{22} & Gyro_{23} \\ Gyro_{31} & Gyro_{32} & Gyro_{33} \end{bmatrix} = \begin{bmatrix} 0.9451 & 0.0197 & 0.0003 \\ -0.0082 & 0.9304 & -0.0097 \\ 0.02 & 0.0427 & 1.0017 \end{bmatrix}$$

$$\begin{bmatrix} Gyro_{10} \\ Gyro_{20} \\ Gyro_{30} \end{bmatrix} = \begin{bmatrix} 5.5561 \\ -12.8228 \\ -0.1553 \end{bmatrix}$$

3.3.6 MAGNOTEMETER

The magnetometer is the least reliable of the sensors since external magnetic fields can easily interfere with the earth's magnetic field. Regardless, gravitational forces alone cannot be used to determine the heading angle, and it is therefore essential to use magnetometer measurements combined with gyroscopic measurements to compute the heading angle. In

order to compute calibration parameters for the magnetometer was rotated about the z-axis, and the heading angle was compared with the angle computed from the gyroscope. The angles computed using the gyroscope. Figure 4-5 illustrates the comparison of heading angles computed using raw and calibrated magnetometer and gyroscope data.

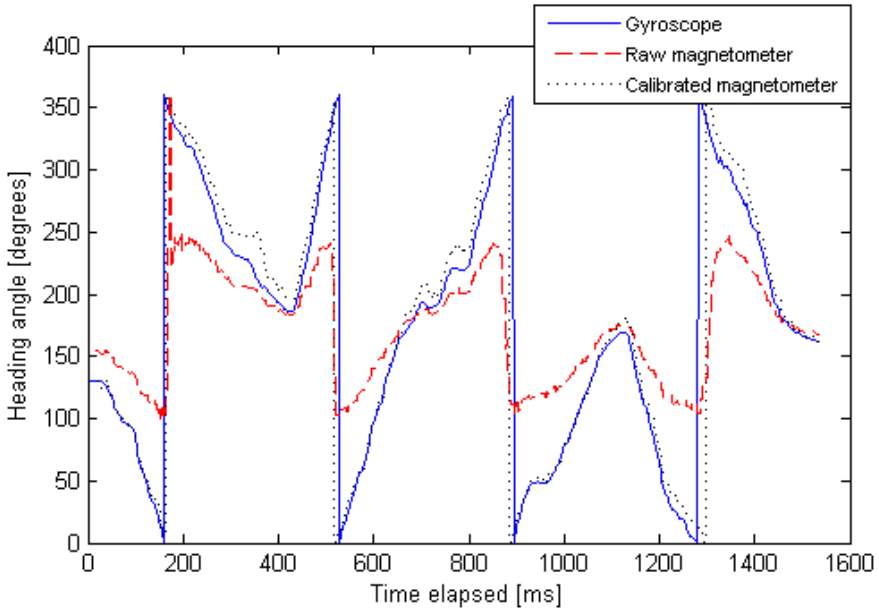

Fig. 3- 5 Comparison of the yaw angle computation using raw and calibrated magnetometer data and gyroscope data

3.3.7 SENSOR NOISE DISTRIBUTION

Once all sensors were calibrated, the *kurtosis* values of the sensor data were compared. Kurtosis is the measure of peakedness of a distribution, and any Gaussian distribution is defined as having a value of 3 **Error! Reference source not found.**. Kurtosis values lower than 3 refer to distributions that have flatter shapes than that of Gaussian distributions. The readout distribution of an ideal sensor is an impulse with a mean at the expected value. Therefore, higher kurtosis values can be associated with more reliable sensors. Table 3-2 shows the kurtosis values of sensors based on 50 000 samples at 100Hz for each sensor axis.

Table 3- 2 Kurtosis values of sensor noise

Sensor axis	**X**	**Y**	**Z**

Accelerometer	67.6616	29.1857	8.8683
Gyroscope	1240	5199	146.7
Magnetometer	4.3924	3.117	3.131

Table 3-2 suggests that all sensor readings have kurtosis values that are higher than 3. Very high kurtosis values observed in gyroscope noise data suggest that they are very reliable in the short term. Long term drift issues associated with gyroscopes were not addressed in this experiment. The magnetometer readings have flatter distributions, which confirm the less reliable measurements.

CHAPTER 4
ENERGY STORAGE SOURCES

4.0 INTRODUCTION

Energy acquired from harvesting and scavenging functions can be accumulated in different storage devices: batteries, supercapacitors and hybrid storage devices such as combination of the both. The selection of appropriate energy storage devices depends on the application requirements, energy harvesting sources, expected life cycle and environmental conditions in which the application needs to operate. Proposed application demands that the energy is provided on constant basis for uninterrupted operation of microcontrollers, sensors, power converters and memories. This chapter highlights and explains different energy storage technologies as well as their competitive advantages and disadvantages, charging protection circuit and operational characterization of the storage element.

4.1 SELECTION OF ENERGY STORAGE

4.1.1 BATTERIES

Batteries are classified by their basic chemistry structure such as lead-acid or lithium-ion. Structure of the battery consists of: Cathode (+), Anode (-) and electrolyte material used to

move the charge between the terminals and it also provides an environment to separate the terminals (Fig 4-1). Batteries are differentiated by the type of rechargeable chemistry employed: nickel-cadmium, lithium-polymer or solid-state thin film . There are many types of battery cells available in a wide range of form factors. Battery packs can be designed to precisely fit into a portable electronic device right from the factory, and are available in standard and familiar cell formats such as AAA, AA, C, or D.

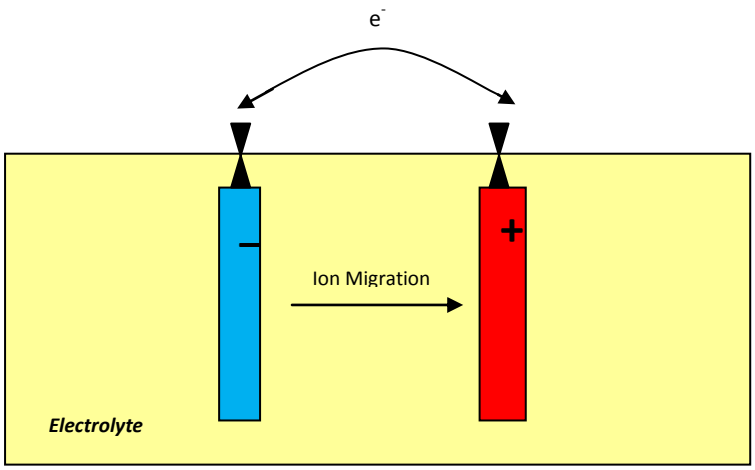

Fig. 4- 1 General battery system

4.1.2 BATTERY PARAMETERS

•***State of Charge*** (**SOC**)(%) – Represents the present battery capacity as a percentage of maximum capacity. SOC is calculated using current integration to determine the change in battery capacity over time.

$$SOC=1 - Q_e/C(0,\theta) \quad (4\text{-}1)$$

• ***Depth of Discharge*** (**DOD**) (%) – The percentage of battery capacity that has been

discharged expressed as a percentage of maximum capacity. A discharge to at least 80 % DOD is referred to as a deep discharge.

$$DOC = 1 - \frac{Qe}{C(Iavg,\theta)} \quad (4\text{-}2)$$

Δ:Qe Charge of battery

Δ: C Battery Capacity

Δ: θ Electrolyte Temperature (^{0}C)

Δ: Iavg Mean Discharge current(A)

• ***Terminal Voltage*** (**V_T**) – The voltage between the battery terminals with load applied. Terminal voltage varies with SOC and discharge/charge current.

• ***Open-circuit voltage*** (**V_{OC}**) – The voltage between the battery terminals with no load applied. The open-circuit voltage depends on the battery state of charge, increasing with state of charge.

• ***Internal Resistance*** (**R_I**) – The resistance within the battery, is generally different for charging and discharging, also dependent on the battery state of charge. As internal resistance increases, the battery efficiency decreases and thermal stability is reduced as more of the charging energy is converted into heat.

• ***Nominal Voltage (V)*** – The reported or reference voltage of the battery, also sometimes thought of as the "normal" voltage of the battery.

• ***Cut-off Voltage*** – The minimum allowable voltage. It is this voltage that generally defines the "empty" state of the battery.

• ***Capacity or Nominal Capacity*** (Ah for a specific C-rate) – The total Amp-hours available when the battery is discharged at a certain discharge current (specified as a C-rate) from 100 percent state-of-charge to the cut-off voltage. Capacity is calculated by multiplying the discharge current (in Amps) by the discharge time (in hours) and decreases with increasing C-rate.

• ***Energy or Nominal Energy*** (Wh) – The "energy capacity" of the battery, the total Watt-hours available when the battery is discharged at a certain discharge current from 100 percent state-of-charge to the cut-off voltage. Energy is calculated by multiplying the discharge power (in Watts) by the discharge time (in hours). Like capacity, energy decreases with increasing C-rate.

• ***Cycle Life*** (number for a specific DOD) – The number of discharge-charge cycles the battery can experience before it fails to meet specific performance criteria. Cycle life is estimated for specific charge and discharge conditions. The actual operating life of the battery is affected by the rate and depth of cycles and by other conditions such as temperature and humidity. The higher the DOD, the lower the cycle life.

• ***Specific Energy*** (Wh/kg) – The nominal battery energy per unit mass, sometimes referred to as the gravimetric energy density. Specific energy is a characteristic of the battery chemistry and packaging. Along with the energy consumption of the vehicle, it determines the battery weight required to achieve a given electric range.

• ***Specific Power*** (W/kg) – The maximum available power per unit mass. Specific power is a characteristic of the battery chemistry and packaging. It determines the battery weight required to achieve a given performance target.

• ***Energy Density*** (Wh/L) – The nominal battery energy per unit volume, sometimes referred to as the volumetric energy density. Specific energy is a characteristic of the battery chemistry and packaging. Along with the energy consumption of the vehicle, it determines the battery size required to achieve a given electric range.

• ***Power Density*** (W/L) – The maximum available power per unit volume. Specific power is a characteristic of the battery chemistry and packaging. It determines the battery size required to achieve a given performance target.

• ***Maximum Continuous Discharge Current*** – The maximum current at which the battery can be discharged continuously. This limit is usually defined by the battery manufacturer in order to prevent excessive discharge rates that would damage the battery or reduce its capacity. Along with the maximum continuous power of the motor, this defines the top sustainable speed and acceleration of the vehicle.

• ***Maximum 30-sec Discharge Pulse Current*** –The maximum current at which the battery can be discharged for pulses of up to 30 seconds. This limit is usually defined by the battery manufacturer in order to prevent excessive discharge rates that would damage the battery or reduce its capacity. Along with the peak power of the electric motor, this defines the acceleration performance (0-60 mph time) of the vehicle.

• ***Charge Voltage*** – The voltage that the battery is charged to when charged to full capacity. Charging schemes generally consist of a constant current charging until the battery voltage

reaching the charge voltage, then constant voltage charging, allowing the charge current to taper until it is very small.

• ***Float Voltage*** – The voltage at which the battery is maintained after being charge to 100 percent SOC to maintain that capacity by compensating for self-discharge of the battery.

• ***Recommended Charge Current*** – The ideal current at which the battery is initially charged (to roughly 70 percent SOC) under constant charging scheme before transitioning into constant voltage charging.

• (***Maximum) Internal Resistance*** – The resistance within the battery, generally different for charging and discharging.

4.2 DIFERENT BATTERY TECHNOLOGIES

4.2.1 Nickel-Cadmium

(NiCd) batteries are characterized by low cost and mature technology and low internal resistance. The internal resistance of the battery limits operating conditions such as temperature and determines the useful life of the battery. Due to Its low internal resistance NiCd batteries are well suited for applications where high power is required for short periods. High discharge currents of up to 50 times the battery capacity (or 50 A for a 1-Ah cell) are easily tolerated and have a minimal effect on capacity [52]. Terminal voltage changes vary slowly as the cell is discharged. NiCd cells do not deteriorate after long periods spent fully discharged. Self-discharge rates are in the range 20% /month at 21˚C. A common NiCd cell size is AA. The Sanyo Cadnica SY115-ND (Fig 4.2) provides 70 mAh capacity at 140 mA (0.2 C rate). Internal

impedance at 50 percent discharge is 16 mΩ (at 1,000 Hz) and charging current can range from 70 mA (standard, 14 to 18 hours charging time) to 1,050 mA (fast, about 1 hour charging time).

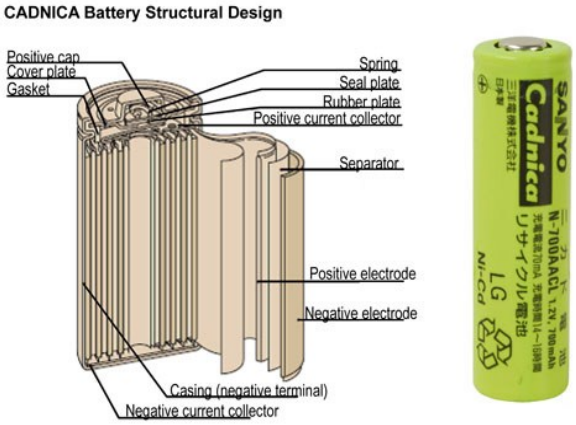

Fig. 4- 2 Structure of the Sanyo Cadnica SY115-ND 700 mAh NiCd AA cell

4.2.2 Lithium and Thin-film

Lithium-ion (Li-ion) cells have two times greater power-to-mass density improvements over NiMH cells. Li-ion cells have a high internal resistance compared with other secondary cells. Their overall cost is declining due to their wide spread usage in hand held and portable devices. Panasonic-BSG, for instance, manufactures lithium cells in very small coin formats in a range of capacities from a few mAh up to 100 mAh at 0.002 C discharge rate (Fig. 4-2). The P088-ND cell achieves this high capacity in a package, 30 mm diameter and 4.2 mm thick, specified to deliver 200 µA for 500 hours. Li-ion cells exhibit a high internal resistance compared with other secondary cells [53]. Li-polymer (often referred to as Li-Po) batteries belong to class of Li-ion cell in which the electrolyte is held within a polymer material. Li-Po cells have improved power output for a given weight compared to standard Li-ion cells. Li-Po batteries are good choice for energy harvesting since due to their high discharge to charge efficiency (greater than 99% vs. less than 90% for standard Li-ion). But while lithium-

Ion/polymer chemistry batteries provide the high-performance features necessary, they must be treated with care. The main disadvantage of the lithium-ion/polymer cells is their risk of becoming unstable if charged over 100 mV beyond their recommended float voltage. Manufacturers' recommendations have to be studied with care before designing the charging and discharging control circuits for all lithium-based secondary batteries.

Fig. 4- 3 Panasonic-BSG P088-ND 100-mAh lithium coin cell

4.2.3 SUPERCAPACITORS

Double-layer capacitors or supercapacitors are commonly used storage element in energy harvesting applications. They are characterized by having a higher power density than batteries, do not require special charging circuitry, and have a long operational lifetime which is usually considered to be unrelated to the number of charge/discharge cycles [54]. Supercapacitors behavior is not ideal and devices exhibit characteristics such as voltage drop and recovery, which occur over very long periods. Supercapacitors have two solid electrodes (in contact with a terminal plate) each with a liquid electrolyte . The area between the solid electrode material and its electrolyte solution, as shown in Fig 4-4, forms the 'double layer'. Due to the fact that charge is stored across a very large effective surface area within the porous electrode, high capacitance values can be achieved in relatively small volumes. As the

charge is stored in the electrolyte, this means that extraction of charge relies on its diffusion, and therefore some processes in supercapacitors have very long time constants.

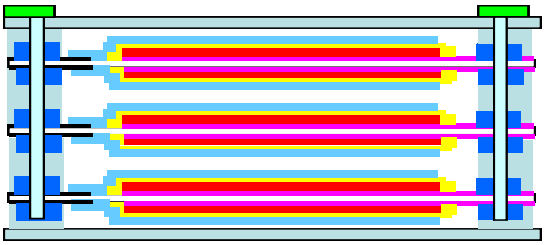

Fig. 4- 4 Supercapacitor cross section

Capacitance C is defined as the ratio of stored (positive) charge Q to the applied:

$$C=\frac{Q}{V} \tag{4-3}$$

Conventional capacitor, C is directly proportional to the surface area A of each electrode and inversely proportional to the distance D between the electrodes:

$$C=\varepsilon_0\varepsilon_r\frac{A}{D} \tag{4-4}$$

The energy E stored in a capacitor is directly proportional to its capacitance:

$$E=\frac{1}{2}\,CV^2 \tag{4-5}$$

Power (P) is the energy expended per unit time. To determine P for a capacitor, it is important to consider that capacitors are generally represented as a circuit in series with an external “load” resistance R. The internal components of the capacitor (e.g., current collectors, electrodes, and dielectric material) also contribute to the resistance, which is measured in aggregate by a quantity known as the equivalent series resistance (ESR). The voltage during discharge is determined by these resistances. When measured at matched impedance (R = ESR), the maximum power Pmax for a capacitor is given by:

$$P_{max} = \frac{V^2}{4xESR} \quad (4\text{-}6)$$

Equivalent circuit has been developed to capture additional Faradaic effects observed in supercapacitors [55]. The schematic of equivalent circuits used to model porous electrodes is presented in Figure 4-5. This final equivalent circuit is known as a transmission line, the distributed resistances represent the ESR intrinsic to each pore as the ions from the electrolyte diffuse towards the electrode.The distributed capacitances represent the non-Faradaic double-layer capacitance of each pore [40, 43]. This equivalent circuit is modeling a porous pseudocapacitor electrode by incorporating the Faradaic pore equivalent circuit [23-24].

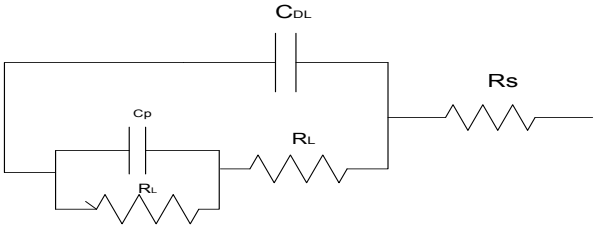

Fig. 4- 5 Equivalent Circuit model of superacapitor

4.2.4 THIN FILM BATTERIES

Thin-film batteries belong to a specific class of lithium-ion cell in which the active surface areas of the electrodes are increased by the reduced dimensions of the components; this translates into more active ingredients with a smaller cell volume. The result is reflected through much higher power and energy density ratings. The electrolyte is solid state. Thin Film Batteries offer advantages over conventional battery systems. Performance advantage is related to the replacement of the liquid electrolyte by a solid one, which limits any leakage, improves thermal stability, and is environmentally friendly. Due to the well-defined solid/solid interfaces, those batteries are stable and less prone to morphological and chemical

modifications (e.g., dendrite formation whenever metal lithium is used as negative electrode, solid/electrolyte interphase at the surface of the negative electrode. Thin film batteries are built layer by layer by vapor deposition. The resulting battery is formed of parallel plates, much as an ordinary battery construction, just much thinner [56]. The figure (Fig 4-6) shows an example of a thin film battery layout where films are deposited symmetrically onto both sides of a supporting substrate. The full stack of films is only 10 to 15 μm thick, but including the support at least doubles the overall battery thickness. When the support is thin, the entire battery can be flexible. Typically the assembled batteries have capacities from 0.1 to 5 mAh.

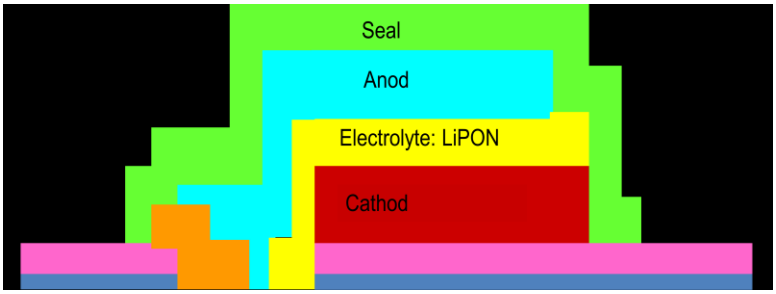

Fig. 4- 6 Thin Film battery architecture

The operation of the thin film battery starts when Li+ ion migrates from the anode to the cathode film by diffusing through the solid electrolyte. If the anode and cathode reactions are reversible, as for an intercalation compound or alloy, the battery can be recharged by reversing the current. The difference in the electrochemical potential of the lithium determines the cell voltage. The active materials used for the thin film cathodes and anodes are based on intercalation compounds. The cycling properties and the overall microstructures resemble those of supercapacitiors, but the microstructures of the thin films may be quite distinct from those of battery electrodes formed from powders. The thin film cathodes are dense and homogeneous with no added phases such as binders or electrolytes. When deposited at ambient temperatures, the films of cathodes, such as $LiCoO_2$, LiMn2O4,

$LiFePO_4$ are amorphous or nanocrystalline. Thin film batteries often act as excellent cathodes with large specific capacities and good stability for hundreds to thousands of cycles. Thin film battery can be represented by the RC model[56].As shown in Figure 4-7, it consists of two capacitors (*C*c, *C*b) and three resistors (*R*t, *R*e, *R*c). The capacitor *C*c, which has a small capacitance and mostly represents the surface effects of a battery, is named surface capacitor. The capacitor *C*b, which has a very large capacitance and represents the ample capability of a battery to store charge chemically, is named bulk capacitor. SoC can be determined by the voltage across the bulk capacitor. Resistors *R*t, *R*e, *R*c are named terminal resistor, end resistor and capacitor resistor, respectively. *U*b and *U*c are the voltages across *C*b and *C*c, respectively. The electrical behavior of the circuit can be expressed by Equations (4-7) and (4-8).

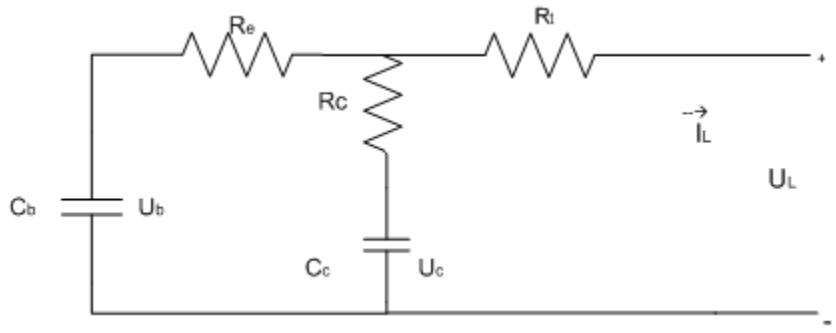

Fig. 4- 7 Schematic diagram of the RC model

$$\begin{bmatrix} Uc \\ Ub \end{bmatrix} = \begin{bmatrix} \frac{-1}{Cb(Re+Rc)} & \frac{1}{Cb(Re+Rc)} \\ \frac{1}{Cc(Re+Rc)} & \frac{-1}{Cc(Re+Rc)} \end{bmatrix} \begin{bmatrix} Ub \\ Uc \end{bmatrix} + \begin{bmatrix} \frac{-Rc}{Cb(Re+Rc)} \\ \frac{-Re}{Cc(Re+Rc)} \end{bmatrix} [I_L] \qquad (4\text{-}7)$$

$$[U_L] = \begin{bmatrix} \frac{Rc}{(Re+Rc)} & \frac{Re}{Re+Rc} \end{bmatrix} \begin{bmatrix} Ub \\ Uc \end{bmatrix} + \begin{bmatrix} -Rt - & \frac{ReRc}{(Re+Rc)} \end{bmatrix} [I_L] \qquad (4\text{-}8)$$

4.3 CYCLE LIFE AND TEMPERATURE EFFECTS

One of the key advantages of thin film batteries with several different cathode and anode materials is their capability to be cycled to thousands of deep cycles with little loss of capacity. This is attributed to the ability of the thin film materials to accommodate changes of a volume associated with the charge-discharge reactions, and with the uniformity of the current and charge distribution in the thin film structure. With cycling, the batteries gradually have tendency to become more resistive with aging rates that depend on the particular electrode materials, the thickness of the films, and the temperature and voltage range during operation of the battery [57]. As all-solid-state devices, thin film batteries can operate over a wider temperature range than most lithium ion batteries. Results of reasonable cycling performance are reported.

Table 4- 1 *Main Characteristics of the thin film battery used in the application*

Capacity (µAh) at 1µA /EFL700A39	2.5
Cycling voltage (V)	2.6-1.7V
Reflow Temperature Tolerance	260^{o}C (3 times)
Package	BGA
Dimension (mm)	5x5
Operating temperature range	-40^{o}C to 150^{o}C

Battery can be charged from a 4.2 V ± 0.05 V constant voltage source with or without

current limit. More than 90% of the total capacity is recharged when the charge current falls below 0.1 mA. When discharging under constant current or constant load, the cut-off voltage can be lowered to 2.0 V for pulsed discharge (Fig. 4.8)

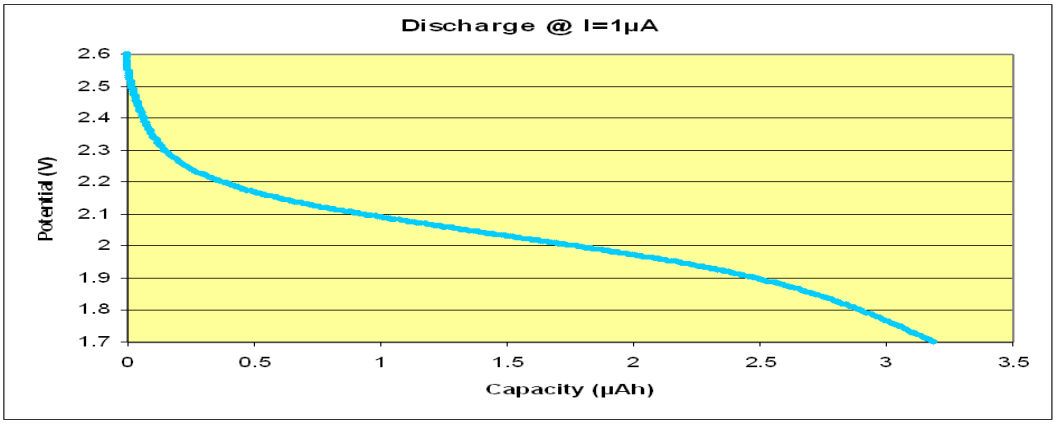

Fig. 4- 8 Typical Discharge Curve

4.3.1 EFFECTS OF THE TEMPERATURE

At low temperature, rates of battery charge and discharge are limited by the thermally activated diffusion and conduction processes, but no permanent damage to the battery occurs from freezing temperatures. When cycled at high temperatures, battery degradation increases and due to gradual microstructure orphase changes in the electrodes or at the interfaces (Fig. 4-9). For example, aging forLiCoO2 cathodes cycled above 75°C is associated with a trigonal to cubic transformation [57].

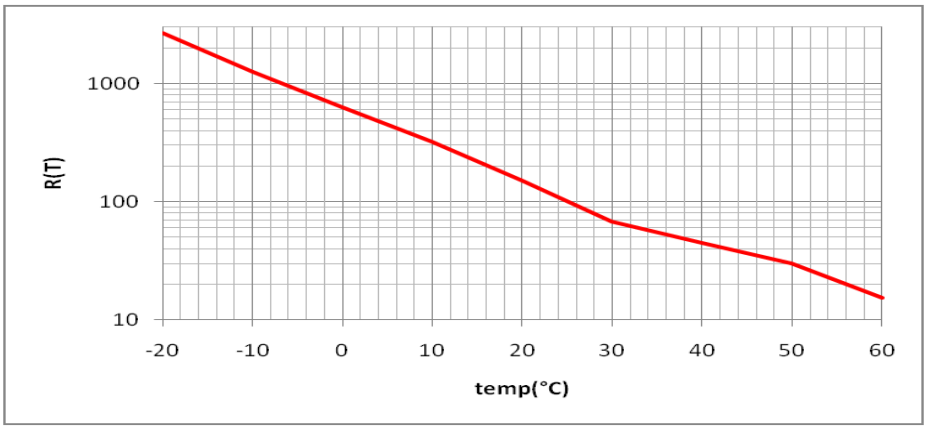

Fig. 4- 9 Resistance vs. temperature

4.3.2 ENERGY AND POWER

The power and energy produced by thin film batteries are dominated by constant discharge of current over a voltage range that gives a full depth of discharge at low currents. Thicker cathodes give proportionally higher energies but often at the expense of the high power performance. The exception is for batteries with the highly conductive $LiCoO_2$ cathode films, where good performance with theoretical capacity utilization has been obtained for batteries made at ORNL with film thicknesses up to 4 μm. Intrinsic stresses in the films, as well as stresses due to electrochemical and thermal cycling, generally limit the cathode film thickness to several micrometers, but companies commercializing the thin film batteries report success in preparing $LiCoO_2$ cathodes well above 4 μm thick.

Table 4- 2 Overview of different battery densities and their properties

Battery Model	**EFL700A39**	**EFL500B39**	**EFL20E3x39**
Architecture	**Single cell**	**Single Cell**	**stack**
Capacity (μAh)	**700**	**500**	**20000**
Cycling voltage(V)	**4.2~3.6**	**4.2~3.4**	**4.2~3.6**
Size (mm)	**25.4 x 25.4 x0.2**	**25.4 x 12.7 x tbd**	**15x15x1.3**
Peak current	**15mA**	**Tbc**	**100mA**

Energy densities for batteries with $LiCoO_2$ cathodes can be discharged at very high continuous and pulsed current densities. They can also be quickly charged at high currents. Charging at steady voltage is the simplest and quickest way to recharge a thin film battery. Batteries with a $LiCoO_2$ cathode can be charged at 4.2 or 4.5 V to >90% full capacity within a few minutes if the charging device can deliver a high current. At the other extreme, thin film batteries can be charged at trickle currents of <1 $\mu A/cm^2$, such as the ones produced by an energy scavenging device. In energy harvesting and scavenging applications, energy efficiency is important. Energy dissipated in the battery charge and discharge is apparent as a

voltage gap between the charge and discharge curve of a battery cycle [56]. For batteries with highly crystalline and reversible electrode materials such as $LiCoO_2$ and LiMn2O4 cathodes with Li anodes, the cycling efficiency at low currents exceeds 96%. For batteries with amorphous cathodes, the energy efficiency is lower even for low current densities because due to the hysteresis in the lithium insertion reaction. In that case the efficiencies may be only 80%. In that case the thin film batteries can be normalized values of energy and power by the active area of the battery because these values do not depend on the choice of substrate and protective packaging. If neglect the substrate and packaging, the active battery components (i.e., the current collectors plus electrode films and Lipon) sum to roughly 3 to 7 mg and 0.7 to 1.5 $\mu L/cm^2$ active area depending on the thicknesses of the active electrode films. In that case a 1 mWh battery would be just 2.5 mg and less than 1μL, so that specific energy and power approach 400 Wh/kg and 1 kWh/L. Under more realistic assumptions where a light-weight substrate and coating are included, the mass and volume of the battery is increased by 2- to 6-fold.

4.3.3 CHALANGES WITH THIN FILM BATTERIES

For many small devices it may be inconvenient or impossible to accommodate a large planar battery area required to meet the energy or power requirements of the device. Stacking multiple cells to limit the footprint is a solution being developed commercially. With relatively thick electrodes, a stack consisting of a small number of thin film batteries connected in parallel can readily match projections of 5 mWh/ cm2 and 3.5 mAh/cm2 proposed for more complex 3-dimensional battery structures. Another solution is to use higher surface area substrates, including fibers29 and sheets with shallow machined ridges and dimples to provide more active area per footprint. These approaches preserve the uniform charge and current distribution of the planar battery architecture. For micro battery packages

of millimeter scale dimensions, efficient connection of many tiny cells in parallel will be needed. Future advances may lead to techniques to stack batteries directly by vapor deposition which will eliminate the volume and mass associated with multiple support layers.

4.4 BATTERY PROTECTION AND MONITORING

The thin film protection circuit monitors the three main battery parameters: voltage, current and temperature, and includes a Coulomb counter to keep track of the charge/discharge status.

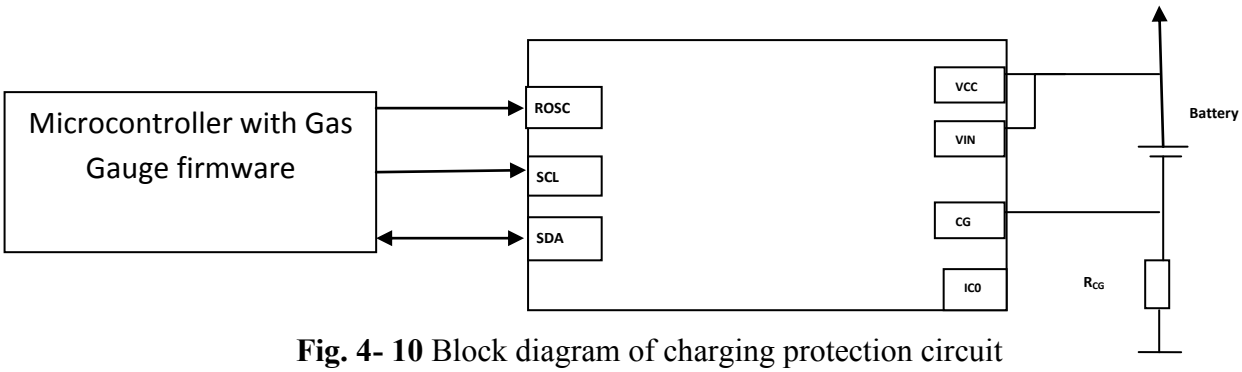

Fig. 4- 10 Block diagram of charging protection circuit

As power needs depend on the demand for energy from the electronics, it can become difficult to manage the battery's state-of-charge (SoC) and predict the remaining operating time with no dedicated gas gauge support. This issue was resolved by using the STC3100, a device that includes battery monitoring features (voltage, current and temperature) and a Coulomb counter to implement a gas gauge (Fig. 4-10). The STC3100 battery monitoring function includes the measurement of the battery voltage and current, measurement of the IC's die temperature and computation of the battery charge variation (Coulomb counter). Figure 4-11 shows voltage versus current for the battery [58].

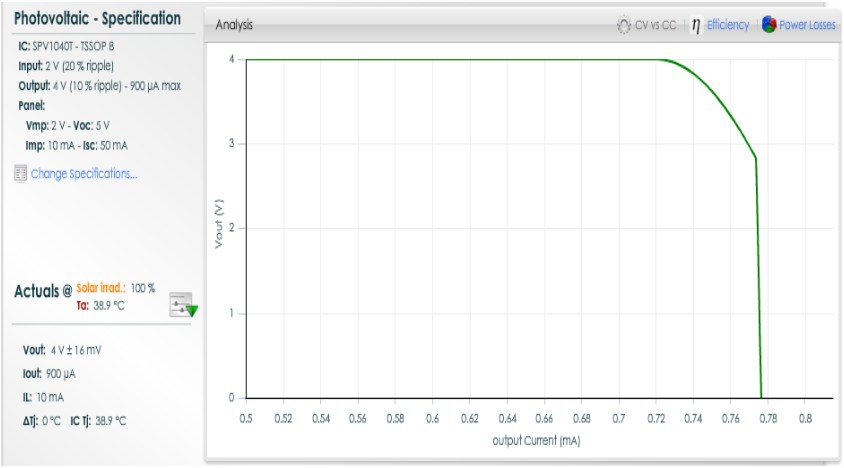

Fig. 4- 11 V vs. Iout

The battery protection circuit uses the battery voltage to estimate the battery's state-of-charge and save it in a RAM location of the STC3100 as a reference value. During subsequent calls, STC3100 the saved reference value and the present charge register content to calculate the present battery capacity:

battery capacity = reference value + charge register content.

If the battery voltage is low (less than 3.1V), the "low battery" alarm is triggered. The setup will than calculate the remaining operating time from the remaining battery capacity and current consumption when the battery is not charging (negative current). The shutdown code puts the STC3100 in standby mode by writing 0 into the REG_MODE register.

The schematic in Figure 4-12 demonstrates the circuit that implements the charge and battery monitoring functions

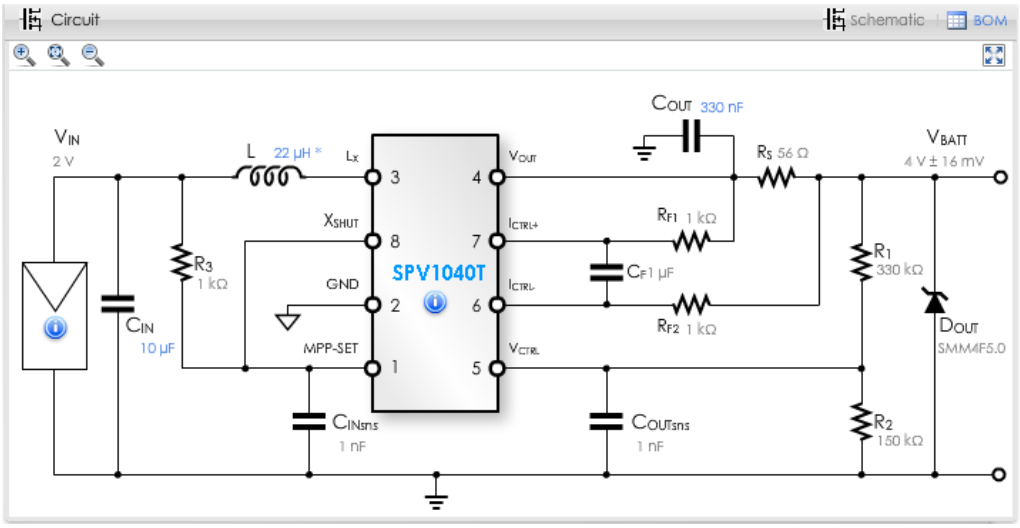

Fig. 4- 12 Demonstration of Battery protection circuit

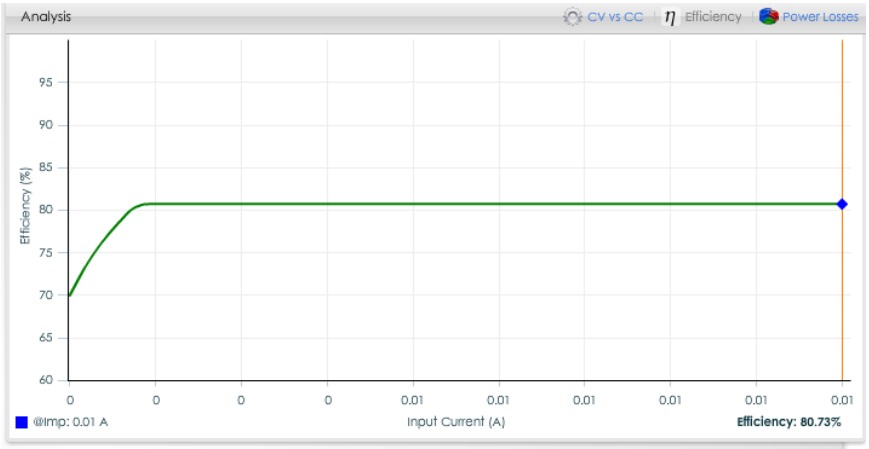

Fig. 4- 13 Efficiency of the battery protection circuit

Efficiency of battery protection circuit is quite important factor due to limited amount of energy available by the harvesters. Efficiency of the battery in the comparison with the cost of replacing the battery due to damage or over usage is a smaller factor in the overall equation. Utilizing the battery protection circuit in overall system will introduce minor inefficiency in the system; however it is a small price to be paid for the robustness of the overall application. Figure 4-13 shows simulation results for the battery charging circuit, which is in the range of 80%.

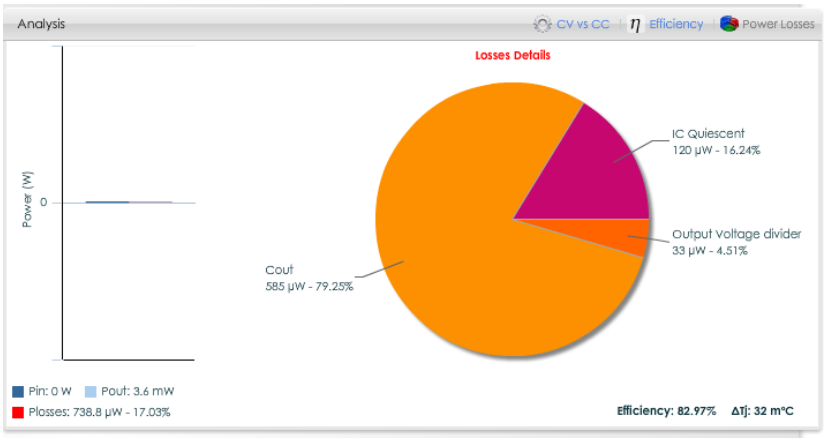

Fig. 4- 14 Distribution of the power loss details in the overall application

Major losses of efficiency are caused by the output capacitors. (Fig. 4-12)

Table 4- 3 Values of biasing components

Type	**Reference**	**Value**	**Description**
IC	IC	SPV1040T	Battery Charger IC &Monitoring
Inductor	L	22uH	2.3A TDK SLF12555T
Capacitor	C_{out}	330nF	10V-20% TDK
Capacitor	C_{IN}	10uF	4V-10% Panasonic
Capacitor	CF	1uF	1uF
Capacitor	CoutSNS	1nF	1nF V rating > 5V
Diode	D_{OUT}	SMM4F5.0	Vbr: 6.8V, V_{Cl}: 9.2V STMicroelectro
Resistor	RS	56Ω	56Ω
Resistor	R3	1 Ω	1 Ω
Resistor	R1	330KkΩ	330kΩ
Resistor	R2	330KkΩ	330kΩ

The overall circuit had to be biased with the capacitors, inductors and the resistors values.

Those values are presented in Table 4-3.

4.5 EXPERIMENTAL MEASSURMENTS

The configuration of the battery test bench is shown in Figure 5-3. The equipment used is to charge/discharge battery module with a maximum voltage of 10 V and a maximum current of 5 A, and can measure in a timely fashion the major parameters like voltage, current and temperature. The host computer with the installed BTS-600 software can program the experimental procedures and deal with real-time data acquisition. In order to limit the temperature's influence on the model parameters, all of the experiments of the thin film battery module were carried out in a thermal chamber with a fixed temperature of 30 °C.

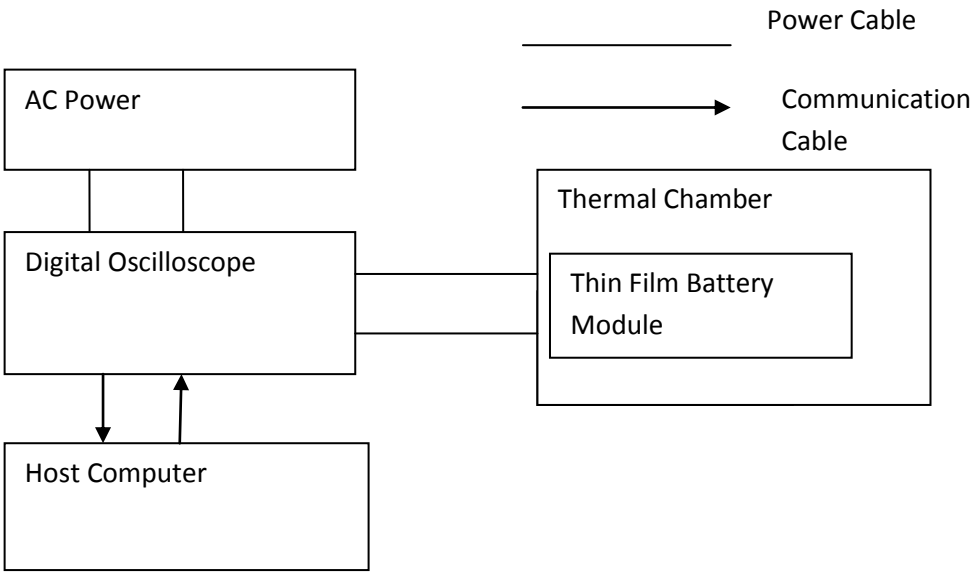

Fig. 4- 15 Experimental setup for measuring the performance if Thin Film battery

Mission profile:

- 50µAh Discharge @ 1C (700µAh)
- 50 µAh Recharge @ 1C (700 µAh)
- 5000 cycles
- T°= 30°C

CAPACITY DRIFT : -0.8%

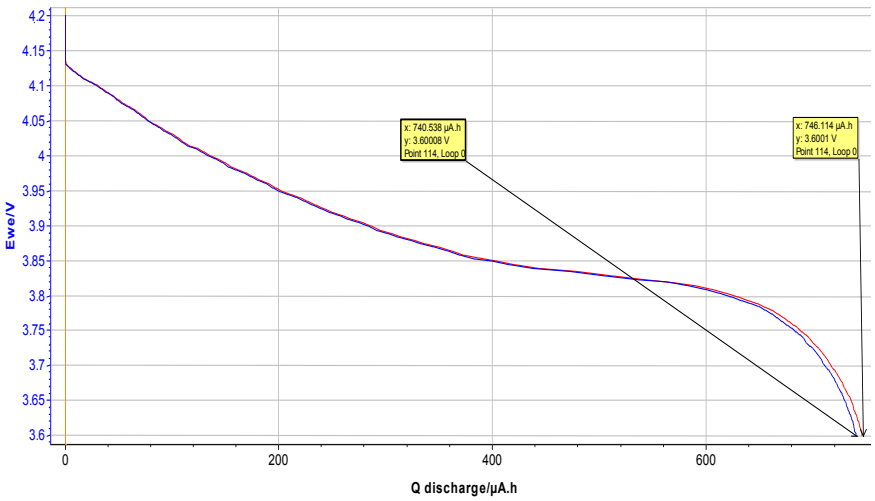

Fig. 4- 16 Capacity drift measurements under the given conditions

RESISTANCE DRIFT : - 2.26%

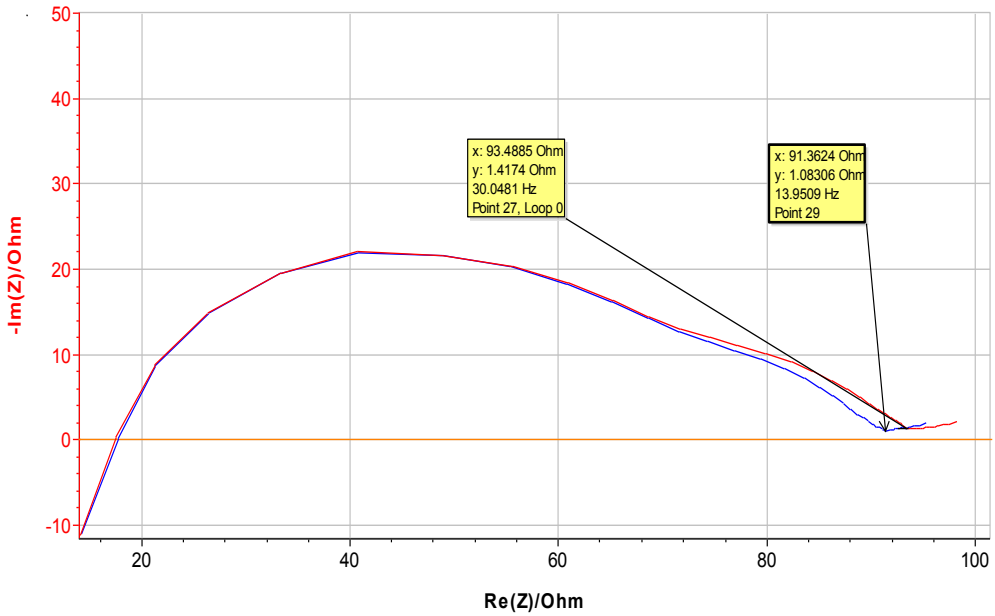

Fig. 4- 17 Resistance drift measurements

Extensive research in the area of energy storage has led to commercialization of storage solutions with advanced properties very suitable for energy harvesting applications. One of

those storage devices are thin film batteries. Applications for thin film batteries include: RFID tags, wireless sensors, medical devices, memory backup power, batteries for extreme high and low temperatures, and energy storage for solar cells and other harvesting devices. Thin film batteries have some challenges and those are: manufacturing challenges, integration with traditional semiconductor processes and the reduction of cost. Investment into new processes will lead to high film deposition rates, reduced processing temperatures, and higher yields. Studies for new thin film materials, in particular for those that can be used as thick anode and cathode films, will improve energy and power densities. Research on materials for effective packaging and electrical connections for multi-cell battery assembly will lead to new and wider markets for use of thin film batteries. The most efficient use of thin film batteries is in a fully incorporated device. The materials that are used to support and protect the thin film battery can also have a dual purpose as an active or protective component of the device. Examples include thin film batteries deposited onto the back of a ceramic integrated circuit chip carrier and thin film batteries deposited on a substrate shared with thin film solar cells. Full integration of the battery and electronic device requires harmonization and compatibility of the fabrication processing which favors an all solid-state battery

CHAPTER 5
ELECTRONIC CIRCUITS FOR ENERGY HARVESTING

5.0 INTRODUCTION

In a case of E-jacket application energy is being harvested from multiple sources: thermal, solar and vibration. In a case of thermal and solar energy sources, the current that is extracted from the energy of DC type and current extracted from the piezoelectric source is of AC type. Since the thermal and the solar sources have DC current, they can be easily interfaced with thin film battery, because the battery has charging protection circuit which in fact is regulating the input from DC sources and making sure that the impedance levels are matched for the maximum power transfer. In a case of piezoelectric harvester, the output current is of AC type and a more complex circuit is necessary to convert the AC current into DC and then to be able to efficiently feed the battery. This type of circuit and the measurement results will be discussed in the following sections.

5. 1 AC-DC CONVERTER FOR PIEZOELECTRIC GENERATORS

Power output of energy harvesting transducers is linked to their size (area, volume). Power management matches load and transducer and cares for maximum energy output. Piezo-transducers provide minimum amounts of charge/current [59]. The topology proposed in the application for piezo electric harvester embedded in E-jacket is based on synchronous buck converter[61]. The switching control is done by low power 8-bit MCU. A vibrating piezoelectric device generates an ac voltage while electrochemical batteries require a dc voltage, hence the first stage needed in an energy harvesting circuit is an ac–dc rectifier connected to the output of the piezoelectric device, as shown in Figure 5-1.

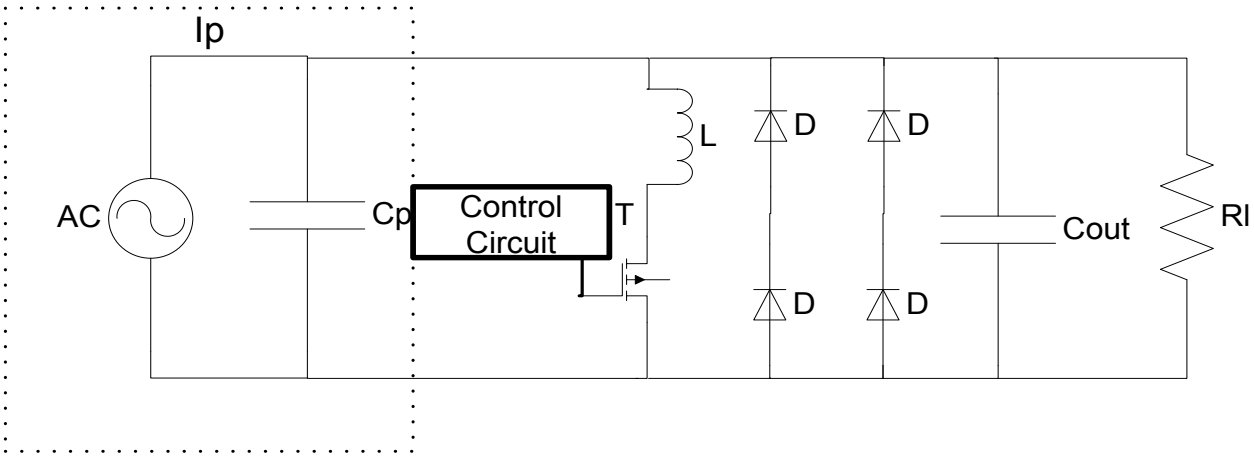

Fig. 5- 1 Synchronized switching harvester

The purpose of this circuit is to maximize the power flowing into the battery. As the battery voltage is essentially constant or changes very slowly, this is equivalent to maximizing the current into the battery. By sensing this current, the duty cycle is adjusted.

The current produced by the rectified piezoelectric element can be related to the change of the element's voltage through the device capacitance during the commutation interval.

$$I_p \sin w = C_p \frac{dv_p}{dt} \qquad (5\text{-}1)$$

During the commutation interval no current flows to the rectifier and the load. Once the piezoelectric element's electrode capacitance is charged to the voltage of the rectifier capacitor voltage, current flows to the load during the remainder of the half-cycle, the interval. During this interval, the output current can be determined by relating the internal piezoelectric element capacitance to the output capacitance

$$I_0(t)=\frac{C_{rect}}{C_{rect}+C_P}+i_p\,(t) \qquad (5\text{-}2)$$

By assuming $C_{rect}>>C_p$ and by solving for the average value of the load current during half of the sine wave, the interval, the load current becomes:

The load current: $$\{I_o(t)\}=\frac{2I_p}{\pi}-\frac{2V_{rect}wC_p}{\pi} \qquad (5\text{-}3)$$

Average output voltage: $$v_0(t)=V_{rect} \qquad (5\text{-}4)$$

Average output power: $$P(t)=\frac{2V_{rect}}{\pi}(I_p-V_{rect}\omega C_p) \qquad (5\text{-}6)$$

The dc–dc converter with an adaptive control algorithm the energy harvesting circuit to be used on any vibrating structure, regardless of excitation frequency, provided a piezoelectric element can be attached [61]

5.2 MEASSURMENT RESULTS

The first test run on the energy management circuit aimed to characterize the performance (Fig. 5-3) shows the charging curve of a 3.3 V thin film battery by the piezoelectric element. To get fully charged it took less than 45 min.

The experimental setup consists of bridge rectifier build from discrete diodes, capacitors and resistors. Piezoelectric element is attached to the demo board in order to provide AC energy which is rectified into DC signal and stored in the capacitor. The purpose of the demonstration is to prove the working concept of full bridge rectifier and piezoelectric as an energy source. Prototype platform is shown in Fig. 5-2.

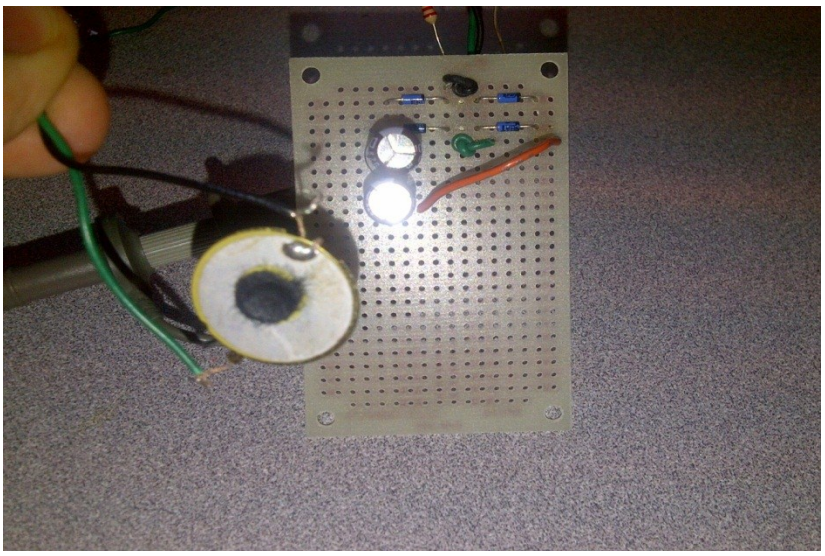

Fig. 5- 2 Prototype platform based on piezoelectric energy harvester

Platform is capable of extracting up to 14V at 1Hz of operation, which is in line with the typical frequency at which the motion of the limbs in the upper section of the body occurs.

Rectifier is converting the AC voltage supplied from the piezoelectric element into a DC voltage which is than stored in two 5000uF capacitors. From Fig. 5-3 it can be seen that 14V DC has been achieved.

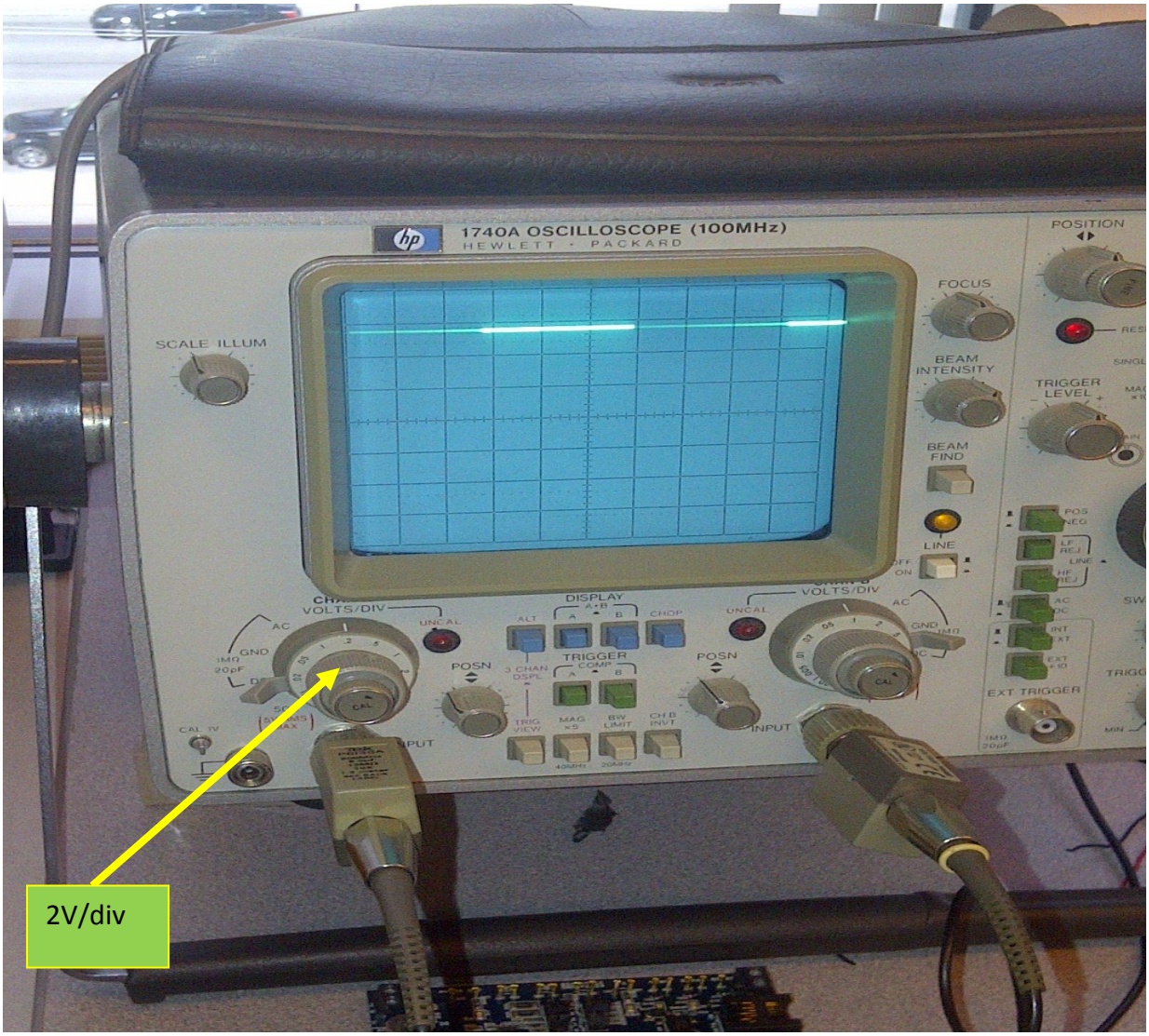

Fig. 5- 3 DC voltage measured from the prototype circuit

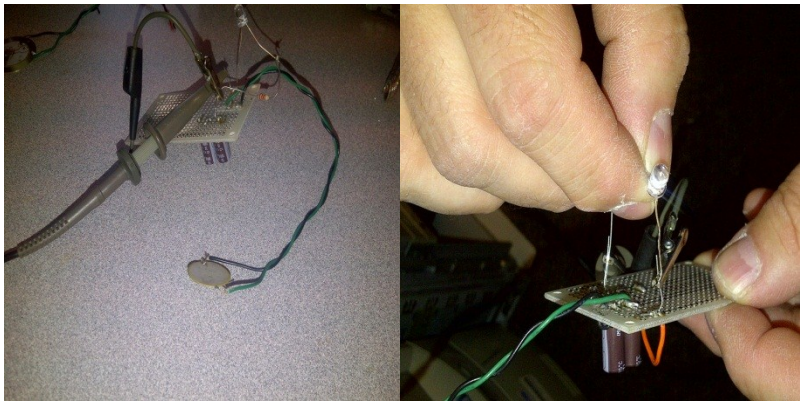

Fig. 5- 4 Experimental set-up and powering of LED

Experimental set-up in Fig. 5-4 is demonstrating that overall circuit topology is generating enough current which to sufficiently power up the LED light. Piezoelectric elements are placed on all the motion sensitive area of E-jacket including shoulder joints, elbow joints and in the center of mass section. With a few hours of activity in the outside environment it is possible to achieve enough energy to power up all the electronic components of the E-Jacket.

5.3 THERMO ELECTRIC ENERGY HARVESTER

Human body emits energy as heat. The temperature difference between the human body and the environment, e.g. low room temperature (20^{O} C) can be harvested. One limitation of TEG's that they produce a very low output voltage, which is in the range of 20mV-200mV, depending on the value of the temperature differential. If we consider that E-jacket is intended for Canadian harsh winter conditions, which on average can provide a temperature difference of 20K., which in return can generate an equivalent power of 12mW. (Fig. 5-5)

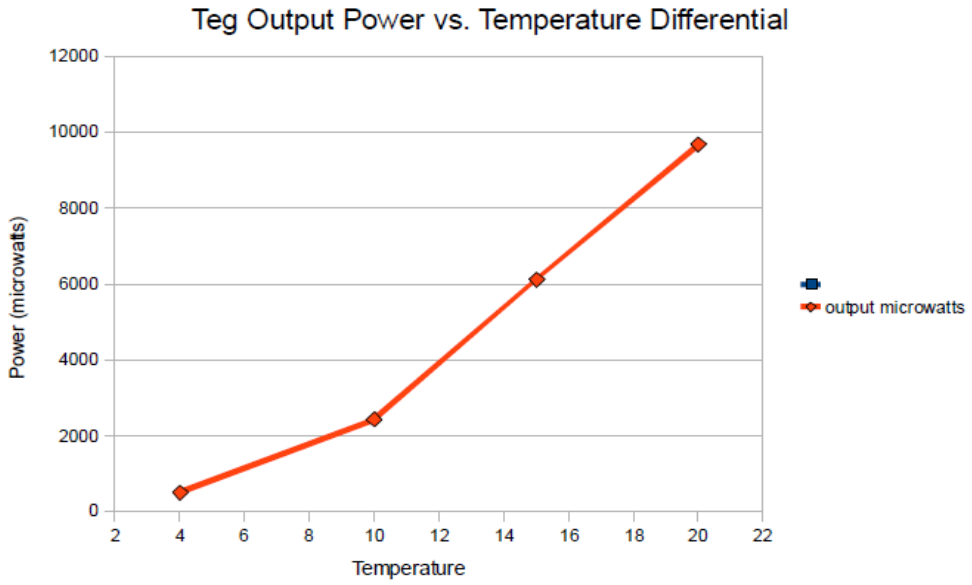

Fig. 5- 5 Measured values of power for different temperature

In order to establish a temperature difference across a thermoelectric device, heat exchangers are needed to extract heat from heat sources and then to dissipate it into ambient [38]. Both the power output and the conversion efficiency of a thermoelectric device increase considerably with increasing temperature difference across it. Efficient heat exchangers are vital to ensure the maximum temperature difference established across the thermoelectric device. In practice, the size, cost, and availability of heat exchangers also need to be considered. It might be necessary to design thermoelectric devices to match the effectiveness of heat exchangers. This is particularly important in the case of energy harvesting from small temperature difference or modules with short thermo elements. In such applications, ΔTHE may still be very large even the available heat exchangers have reached their performance limit. An alternative is to design modules with a relative large $(1 + ZTM)K$.

5.4 OVERALL SYSTEM DEMONSTRATION

Multiple energy sources have advantage, because they are able to acquire power for longer time and in difficult weather conditions. This study has been focused on three different sources of energy: motion, solar and heat. None of the three energy sources are capable of generating enough power needed to operate electronic components that are part of this study, however combining them together has generated very promising results. Out of all three energy sources, motion generates the most amount of power; however this type of power needs to be converted from AC into DC and through a conversion process there is also associated power loss and in this application it is in the range of 18%. Solar and heat energy scavengers are generating a DC voltage and their advantage is evident in ability to generate power in steady state and power that can be directly stored in thin-film battery. In order to optimize the power transfer from heat or solar energy harvester to the battery, it is necessary to design a very efficient charging circuit which has been discussed in Chapter 4. Overall system is capable of supplying 8mA of current which is sufficient to drive on board sensors, low power NFC radio and ultra-low power 32-bit microcontroller. Fully functional system is presented in Fig. 5-6, where STM32-L Discovery board is powered up from the energy that was harvested by motion, body heat and solar energy.

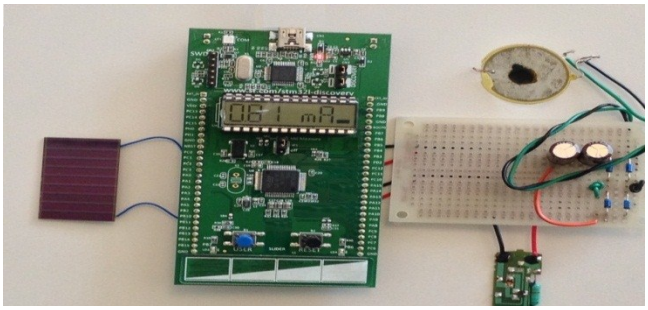

Fig. 5- 6 Full system demonstration with measured current on display

CHAPTER 6
CONCLUSION AND FUTURE WORK

6.0 SUMMARY

In the last ten years the area of energy harvesting has experienced a tremendous growth. This trend has been driven by the three main factors: drastic increase in energy prices, demand for information and demand for autonomy in operation of traditional electronics. Although cost and quality of energy are two significant interposers that provide interface between the economic growth and evolution of human kind, many other new opportunities are driving a trend of energy harvesting as well. Significant improvements in semiconductor industry in respect to the size, performance and cost have opened up a range of new horizons in a lifestyle necessities. Energy abundance means freedom, however energy is also an enabler into a space of cyber physical, wireless sensor networks, internet for things, smart skin and etc.

6.1 ENERGY HARVESTING TODAY

Energy can be acquired through the following harvesting sources: photovoltaic, short range induction, electro-chemical reaction, piezoelectric, magnetic, thermoelectric and electrodynamics. Each of those energy harvesters, has its advantages and limitations, however if combined in a hybrid solution advantages in an overall solution exceed the limitations. Another very important aspect of overall energy harvesting systems is energy storage. Overall role of a storage element within energy harvesting systems in not only manifested in its ability to store harvested energy, but also in the ability to condition and

improve the quality of power that is coming out of energy harvester, this conditioned power is than supplied to the external electronics devices.

6.2 E-JACKET SYSTEM FUNCTIONAL ASPECTS

This thesis is proposing a development of an E-Jacket application intended for recording and monitoring of basic human activity and conditions. A review of the basic human activity monitoring which includes: motion monitoring, motivations, issues and devices and techniques were given. The state-of-art ultra-low power radio with embedded EEPROM memory was analyzed from the hardware standpoint and the main energy harvesting techniques were described. The rest of the thesis has addressed the hardware and software design of the complete monitoring system that is intended to be self-sufficient by using the energy obtained from human body and the environment. Power supply for a E-Jacket consists of an energy harvesting solutions based on thermal, photovoltaic (PV) and piezoelectric energy harvesting elements. The storage solution is based on a stackable thin film battery with external overcharge protection circuit added for the purposes of protecting the state of the battery and an improvement in signal condition. E-Jacket features include multiple sensors mounted on the fabric: temperature sensor, pressure sensor, motion sensor module, EEPROM memory with ultra-low power NFC radio. The radio device is based on Near Filed Communication (NFC) protocol that is ultra-low power and operates at frequency 13.56MHz. This particular radio implementation has its advantages, because most of the toady's smart phones have NFC radio reader build in. This means that all the data in regards to activity monitoring done by the "Smart Jacket", can be transferred to smart phone via NFC and by using wirelessly the power from the smart phone to do that action. The energy-aware solution

implemented in the “Smart Jacket” optimizes the use of the energy and maximizes the time available for computation. The prototyping and testing results were positive and demonstrated how the design of the multi energy harvesting system can be successfully integrated with multiple sensors and NFC radio to construct an application well suited for multi utility role.

6.3 CONCLUSION ON HUMAN POWER

Human power when combined with external abundant source is an attractive option for powering long term wearable sensor modules. Human motion provides an13.56M energy source that is obtained from vibration spectra and human heat. Practical scavenger centered on 2 Hz or resonance peak would be expected to operate well despite slight frequency shifts and would be able to deliver 1.2 mW of power while walking. Power collection to allow storage in a practical battery remains challenging – today’s circuit designs are at 80-90 % efficient.

6.4 CONCLUSION ON PHOTOVOLTAICS

Photovoltaics are the most popular form of energy harvesting. It will continue to keep the leadership spot, because its traditional benefits of being low cost, being thin, having no moving parts, light weight, fairly efficient, and generating conveniently low voltages will be further improved. New initiatives are focused on the printed, tightly rollable, transparent versions and ones that use UV and IR as well. Most popular forms today are cSi, aSi on land and Ge-GaAs in space. Especially of interest for “Smart Jacket” application are Woven photovoltaic. Those PV’s are based on Organic Photovoltaics and on Dye Sensitive Solar Cells-DSSC. Today DSSC fibers are measured to have 7% efficiency.

Significant research work is being done in the following areas for PV's:

- Edible
- Biodegradable
- Printed on paper
- Spray painted onto objects
- Working from ultraviolet, visible and infrared

6.5 CONCLUSION ON VIBRATION HARVESTING

"33" mode produces 4 times more harvested energy than "31" mode. For closed circuit with AC-DC converter (rectifier) and energy storage modules, a "33" mode multilayer stack can harvest orders of magnitude more energy than a bar/beam of the same size if: The peak value of the generated voltage is significantly (5~10 times) larger than the diode forward voltage of the rectifier. The number of layers for a piezoelectric structure should be chosen based on the number of charges passing through the rectifier, i.e., governed by the level of generated voltage and the property of the electrical load applied. High energy efficiency high performance piezoelectric energy harvesters can be developed based on the comprehensive considerations. Piezoelectric converters offer tremendous potential in micro-scale energy harvesting, however additional research must be done concerning fatigue characteristics and scalability towards implementation on a silicon chip. To realize this, efforts must be focused to improve the thin-film PZT process.

6.6 IMPROVMENTS NEEDED FOR TEG

Thermoelectrics is the fourth most popular form of energy harvesting. It uses the Seebeck effect to generate electricity from temperature difference. It has been tried in the Seiko Thermic watch.

Design Targets for TEG:

- Optimization of the thermal flux between TE elements and tubes
- Improvement of reliability through thermal and mechanical stress control
- Focus on light-weight, size and manufacturability.

An improvement in the efficiency of the TEG's can be achieved by the modifications done at the nanoscale level, i.e. by introduction of phonon scattering. When atoms heat up, their electrons will spin and move faster and farther. If they have enough energy, the electrons will move to the neighboring atom, bringing this atom the additional energy it carries thus conducting thermal energy.

6.7 CONCLUSION ON CIRCUIT OPTIMIZATION

Besides general semiconductor industry trends that are driving overall size, cost and power consumption, there are additional steps that can be done in a design of IC components that are used for power management of many energy harvesting applications. Switching power for a CMOS gate working in a synchronous environment is modeled by the following equation:

$$P_{switching}=\frac{1}{2} C_L \, Vd^2 f_{clk} E_{sw}$$

where C_L is the output load of the gate, V_D is the supply voltage, f_{CLK} is the clock frequency and E_{sw} is the switching activity of the gate, defined as the probability of the gate's output to make a logic transition during one clock cycle.

Reductions of $P_{switching}$ are achievable by:

- supply voltage scaling
- frequency scaling
- minimization of switched capacitance

A lot of attention needs to be attributed to a careful selection of a circuit style: static vs. dynamic and synchronous vs. asynchronous. The clock signal in synchronous logic contains no information; therefore, power associated with the clock driver and distribution network is in some sense wasted. Avoiding this power consumption component might offer significant benefits. In addition, asynchronous logic uses completion signals, thereby avoiding glitching, another form of wasted power. Finally, with no clock signal and with computation triggered by the presence of new data, asynchronous logic contains a sort of built in power-down mechanism for idle periods. Traditional technology driven IC technique include: technology scaling, supply voltage reduction, threshold voltage reduction, layout level optimization.

6.8 CONCLUSION ON FIRMWARE OPTIMIZATIONS

Electronic systems consist of hardware platforms with several software layers. Multiple system features depend on the hardware/software interaction, e.g., programmability and flexibility, performance and energy consumption. Software does not consume energy “per se”, but it’s execution and storage are the ones that require energy consumption by the underlying hardware. Thus, software execution involves power dissipation for computation, storage, and communication. Energy efficiency in an operating system can be achieved by designing an energy aware task scheduler. Usually, a scheduler determines the set of start times for each task. Since tasks are associated with resources having specific energy models, the scheduler can exploit this information to reduce run-time power consumption. Also reducing the size of the instruction set will reduce the size of registers and that will results in less power consuming device as well

Appendix A: MPPT Code

```
#include <P16F873A.h>
#include <datalib.h> // RS232 Routines
#include <Strings.h> // iPrtString Function
#include <delays.h>
#asmline __CONFIG 0x393A
// Enable Quick Interrupts
const int QuickInt=1;
enum {T1Overflow=1, ADConversion=2}; // Timer 0 Overflow, A/D Conversion Complete
unsigned char IntFlags; // Interrupt Flags
unsigned int DutyCycle[8]; // PWM Duty Cycle (0 to 1024)
unsigned int Voltage[4]; // Total amount of Voltage samples ([0] counts as one)
unsigned int Current[4]; // Total amount of Current samples ([0] counts as one)
unsigned long Vavg;
unsigned long Iavg;
unsigned long varlong;
unsigned char SampleNum; // Current Sample Number
signed int Power[8]; // Current Power Sample
signed int Powerdiff; // Difference between Power samples
signed int DCdiff; // Difference between DutyCycle samples
signed int Derivative;
signed int DerivativeZ1;
signed int der_acc;
char SerString[7];
void main(void); // Main loop
void initialize(void); // Initial Setup
void interrupt(void); // Interrupt Handler
void ADSample(void); // Converts 2 A/D channels to Voltage and Current values
void AverageVC(void); // Averages voltage and current A/D samples
void PWMout(void); // Update PWM duty cycle
void PWMSweep(void); // Sweep PWM Duty Cycle from 0 to 100%
void RS232Display(void); // Display PWM - Power
void RS232Out(void);
void Control(void); // Control algorithm
const long SERIALRATE_IN=19200;
const int BITTIME_IN=(APROCFREQ)/SERIALRATE_IN/4;
const unsigned char SERIALPORT_IN=&PORTC;
const unsigned char SERIALBIT_IN=7;
// Set up Serial Port Out on Port C Bit 6
const long SERIALRATE_OUT=19200;
const int BITTIME_OUT=(APROCFREQ)/SERIALRATE_OUT/4;
const BYTE SERIALPORT_OUT=&PORTC;
const BYTE SERIALBIT_OUT=6;
//
// USER DEFINED PARAMETERS
//
char Kd=4; // Derivative gain Kd of control system
const unsigned char bksamp=1; // Back sample to sample number bksamp
const unsigned char MODE=1; // MODE=0 Controller specifies DC
// MODE=1 Sweep DC
// MODE=2 Constant DC
const unsigned char DEBUG=1; // DEBUG=1 Debug mode (RS232 Out)
```

```
// DEBUG=0 Production mode (No debug info)
//
// ------------------------------------------------------------------------------------------
----------------------------------------------------------
//
//********MAIN PROGRAM**********//
void main(void)
{
initialize();
while(1)
{
if (IntFlags&=ADConversion); // A/D Interrupt Occured (26.2ms)
{
ADSample(); // Sample the V and I inputs
if (SampleNum==4) // Takes 4 samples of V and I
{
INTCON=0x00; // Disable all interrupts
RS232Display(); // Display information through RS232
#if MODE==1 // MODE = Sweep DC
PWMSweep(); // Change RS2323 Display to DutyCycleZ (not Z1)
PWMout();
#endif
#if MODE==2 // MODE = Constant DC
DutyCycleZ=0x01AE;
PWMout();
#endif
Wait(50); // Delay 50ms
AverageVC();
Control();
#if MODE==0 // MODE = Derivative Controller
PWMout();
#endif
INTCON=(1<<GIE)|(1<<PEIE); // Enable all interrupts
}
IntFlags&=~ADConversion; // Reset A/D Flag
}
} // End While Loop
} // End Main Function
void ADSample(void) // Sample RIGHT justified in ADRESH:ADRESL
{
unsigned int Chan1; // Channel 1 of A/D (Left Justified 10 bits)
unsigned int Chan3; // Channel 3 of A/D (Left Justified 10 bits)
218
if (~ADCON0&(1<<CHS1)) // If A/D conversion is Channel 1
{ // Chan 1 = Voltage
Chan1=ADRESH; // Place high and low byte of AD sample into Chan1
Chan1<<=8;
Chan1|=ADRESL;
#asmline BSF ADCON0, CHS1 ; Clear Channel 1, Set Channel 3
Voltage[SampleNum]=Chan1; // Set voltage value to chan1 A/D
}
else // If A/D conversion is Channel 3
```

```
{ // Chan 3 = Current
Chan3=~ADRESH&0x03; // Place high and low byte of AD sample into Chan3 for current
Chan3<<=8; // Invert ADRESH and ADRESL since hardware is inverted
Chan3|=~ADRESL;
#asmline BCF ADCON0, CHS1 ; Clear Channel 3, Set Channel 1
Current[SampleNum]=Chan3; // Set current value to chan3 A/D
SampleNum++; // Increment Sample Number
}
} // End of ADConv function
void AverageVC(void)
{
for(SampleNum=1; SampleNum<=3; SampleNum++) // 1 to (Total Samples - 1)
{
Voltage[0]+=Voltage[SampleNum]; // Add up 8 samples and put in Voltage[0]
Current[0]+=Current[SampleNum]; // Add up 8 samples and put in Current[0]
}
SampleNum=0;
Voltage[0]>>=2; // Divide by 8
Current[0]>>=2; // Divide by 8
}
void Control(void)
{
// Conversions:
// Voltage: 7 volts = 1024 * x x = 1 / 51.2
// Current: 0.004 Amps = 1024 * y y = 1 / 256
// Power = V * I x * y = 1 / 13056
unsigned long varlong;
unsigned char i;
for (i=7; i!=0; i--)
{
Power[i]=Power[i-1]; // Copy samples to memory
}
DerivativeZ1=Derivative; // Copy sample to old sample for when Der is zero
Vavg=Voltage[0]; // Copy integer to long
Iavg=Current[0]; // Copy integer to long
varlong=Voltage[0]*Current[0];
varlong=Vavg*Iavg; // Multiply long types
Power[0]=0;
Power[0]|=varlong>>5; // PowerZ is 15 bits

Powerdiff=Power[0]-Power[bksamp]; // Diff is full 15 bit integer. 4A * 20V = 80W
DCdiff=DutyCycle[0]-DutyCycle[bksamp]; // DC Diff = 15 bit
//Derivative = ((Powerdiff<<2)/(DCdiff>>5));
Derivative=((Powerdiff<<2)/(DCdiff>>5));// PowerDiff is 15 bit<<2=17bit, DCdiff is 10 bit
// DC is shifted to 10 bit because that is max resolution of PWM out
// Max derivative is 20W/1DC
der_acc+=Derivative; // IIR Filter
der_acc>>=1; // Divide by 2
Derivative=der_acc;
//DutyCycle[1]=DutyCycle[0]; // Before writing new DC, save current DC to old DC
for (i=7; i!=0; i--)
{
```

```
DutyCycle[i]=DutyCycle[i-1];
}
//#if MODE==0
Derivative *= Kd; // Derivative GAIN
if (DCdiff==0)
{
if (DerivativeZ1&(1<<15)) Derivative=-128;
else Derivative=128;
}
DutyCycle[0] += Derivative; // DC 15 bit
if (DutyCycle[0]&(1<<15)) DutyCycle[0]-=Derivative;
// If Duty Cycle rolled around either forward or backwards - subtract that derivative back
out
//#endif
}
void PWMout(void)
{
unsigned varint;
varint=DutyCycle[0]; // Get the 15 bit version of Duty Cycle
varint>>=7; // Make 15bit DC to 8 bit PWM out
CCPR1L=(varint>>2); // Set the PWM 8 MSB from DutyCycle (10 bit)
CCP1CON&=~0x30; // Clear bits 4 and 5 of CCP1CON (2 LSB of PWM)
CCP1CON|=((varint&0x03)<<4); // OR 2 LSB of DutyCycle into 2 LSB of PWM
}
void PWMSweep(void)
{
//DutyCycle[0]=DutyCycle[0]+32;
DutyCycle[0]=0x4000;
if (DutyCycle[0]&(1<<15)) DutyCycle[0]=0x00; // if DutyCycle = 1024 (max resolution)
}
void RS232Display(void)
{
SerString=0;
#if MODE==0 // Mode = Controller
iPrtString(SerString, DutyCycle[1]);
#else // Mode = PWM Sweep OR Constant DC
iPrtString(SerString, DutyCycle[1]);
#endif
RS232Out();
#if MODE==0
SerString=0;
iPrtString(SerString, Power[0]);
RS232Out();
#else
SerString=0;
iPrtString(SerString, Power[0]); // PowerZ1 = PowerZ in Control Function
RS232Out();
#endif
SerString=0;
iPrtString(SerString, Voltage[0]); // Voltage[0]
RS232Out();
SerString=0;
```

```
iPrtString(SerString, Current[0]); // Current[0]
RS232Out();
SerString=0;
iPrtString(SerString, Derivative); // Derivative of sweep is before Kd and Shift
RS232Out();
pSerialOut(0x0D); pSerialOut(0x0A); // New Line
#if DEBUG==1
if (~PORTA&(1<<4))
{
pSerialOut(0x3E);
Kd=pSerialIn();
Kd-=0x30;
pSerialOut(0x0D; pSerialOut(0x0A);
}
#endif
}
void RS232Out(void)
{
unsigned char i;
i=0;
while(SerString[i]!=0) // While String still has characters in it
{
pSerialOut(SerString[i]); // Send them out one by one
i++; // Increment character counter
}
pSerialOut(0x09); // Tab between fields
}
void initialize(void)
{
// Configure the PWM Module
PR2=0x3F; // Set the PWM period to 19.53kHz (max resolution 10.0 bits) PR2=3F (78.12k)
CCP1CON&=~0x03; // Clear 2 LSB of Duty Cycle
CCPR1L=0x00; // Set inital PWM to 0%
TRISC&=~(1<<2); // Set PWM pin for output (RC2/CCP1)
T2CON=0x04; // Turn PWM Module ON; Turn Timer2 On; Set prescale to 1
TMR2=0x00; // Timer2 (PWM) prescale value=1
CCP1CON|=0x0F; // Set CCP1 Mode Select Bits to PWM
// Set RS232 Out Pin
TRISC&=~(1<<6));
// Configure the A/D Module;
PIR1&=~1<<ADIF; // Clear ADIF bit
PIE1|=1<<ADIE; // Set ADIE bit
ADRESH=0; // Clear A/D Registers
ADRESL=0;
TRISA|=0x1B; // Set PORTA<0,1,3,4> to inputs
ADCON0 = 0x89;
// Fosc/16 for 10Mhz. Set A/D on Channel 1 (RA1) A/D Module powered up
ADCON1=0x84; // Set up Port A for Analog: DDDDADAA with Vref+/- to Vdd and Vss
// Set Format: Right Justified 10bits to ADRESH:ADRESL
ADCON0 |= ADON; // Start A/D Converer module (ADON Bit)
// Configure Timer 1 for A/D conversion triggering (using Timer 1 so Timer 0 can be used
for WDT)
```

```
PIR1&=~1<<TMR1IF; // Clear Timer 1 Interrupt Flag
PIE1|=1<<TMR1IE; // Set Timer 1 Interrupt Enable
T1CON=0x10; // Timer 1 Prescale = 1 (Speed set to 1/Fosc*4 * Prescale * 65535) = 26.2mS
// 20Mhz T1CON=0x10 10Mhz T1CON=0x00
TMR1H=0x00;
TMR1L=0x00;
T1CON|=0x01; // Turn Timer 1 On
INTCON=(1<<GIE)|(1<<PEIE); // Enable Interrupts
// GIE: General Interrupts
// PEIE: Peripheral Interrupt Enable
#if MODE==0 // Mode = Controller
Power[0]=0x00C8;
Power[1]=0x00C8;
Power[2]=0x00C8;
Power[3]=0x00C8;
Power[4]=0x00C8;
Power[5]=0x00C8;
Power[6]=0x00C8;
Power[7]=0x00C8;
DutyCycle[0]=0x2000;
DutyCycle[1]=0x2000;
DutyCycle[2]=0x2000;
DutyCycle[3]=0x1810;
DutyCycle[4]=0x1810;
DutyCycle[5]=0x1810;
DutyCycle[6]=0x1810;
DutyCycle[7]=0x1810;
#else // Mode = PWM Sweep
DutyCycle[1]=0x0000;
DutyCycle[0]=0x0000;
#endif
} // End of Initialize function
//
//******************INTERRUPT HANDLER**********************//
//
void Interrupt() // An interrupt occured. Find out what it was
{
if (PIR1&(1<<TMR1IF)) // Timer 1 to trigger an A/D Conversion
{
// Automatically resets TMR1H/TMR1L to 0
PIR1&=~1<<TMR1IF; // Clear Timer 1 Interrupt Flag
//IntFlags|=T1Overflow;
ADCON0|=1<<GO; // Trigger an A/D Conversion
}
if (PIR1&(1<<ADIF)) // A/D Conversion is complete
{
PIR1&=~(1<<ADIF); // Clear the interrupt flag
IntFlags|=ADConversion; // Set user defined interrupt flag
}
} // End of Interrupt function
```

Appendix B: Motion Detection Code

```
from struct import unpack_from
import sys

#serial port
import serial
import io

from direct.showbase.ShowBase import ShowBase
from direct.task import Task
from direct.actor.Actor import Actor
from direct.interval.IntervalGlobal import Sequence
from panda3d.core import Point3

class RotateApp(ShowBase):
    def __init__(self):
        ShowBase.__init__(self)

        # Load the environment model.
        self.environ = self.loader.loadModel("models/environment")
        # Reparent the model to render.
        self.environ.reparentTo(self.render)
        # Apply scale and position transforms on the model.
        self.environ.setScale(0.25, 0.25, 0.25)
        self.environ.setPos(-8, 42, 0)

        # Add CameraTask and Spin procedures to the task manager.
        self.taskMgr.add(self.CameraTask, "CameraTask")
        self.taskMgr.add(self.DizzyFix, "DizzyFix")

        # load and transform the panda actor
        self.spinActor = Actor("models/DizzyFixActor", {"DizzyFix":
"models/DizzyFixActor1"})

        self.spinActor.setScale(0.3, 0.3, 0.3)
        self.spinActor.reparentTo(self.render)



    # Define a procedure to detect motion.
    def MotionTask(self, task):
        self.camera.setPos(0, -20, 3)
        return Task.cont


    # Define a procedure to read serial data and set roll, pitch, yaw
    def DizzyFixTask(self, task):
        s = serial.Serial('com10',9600, timeout=0.03)
        buff = s.read(20000000)

        rf_packets = []
        for i in range(len(buff)/4):
            rf_packets.append(unpack_from("f",buff,i*4)[0])

        # each rf_packet is 16 bytes:
        # first 4 bytes -- preamble and commands
```

```
        # next 12 bytes -- (float) roll, pitch, yaw

        i = 0
        collect = 0
        rpy = [0, 0, 0] # vector to hold roll, pitch, yaw

        for item in rf_packets:

            # first item is 1.1062e-39 as it contains bits for
            synchronization and commands
            if item > 1.1062186389011544e-40 and item <
            1.1062186389011544e-38:
                collect = 1
            else:
                if collect == 1:
                    rpy[i] = item
                    i = i+1

                if i == 3:
                    i = 0
                    collect = 0

            # set pitch, roll, and yaw
            self.spinActor.setHpr(rpy[2], rpy[1], rpy[0])

        return Task.cont

app = DizzyFixApp()
app.run()
```

References

[1] Guyomor, D.; Badel, A.; Lefeuvre, E. and Richard, C. Toward energy harvesting using active materials and conversion improvement by nonlinear processing. IEEE Trans. Ultrason. Ferroelectr. Freq. Control, 52(4), 2005, pp.584-595.

[2] Lay-Ekuakille, A.; Vendramin, G.; Trotta, A. and Mazzotta, G. Thermoelectric generator design based on power from body heat for biomedical autonomous devices. In: IEEE international workshop on medical measurements and applications (MeMeA 2009), Cetraro, Italy, May 29-30 2009, pp.1-4.

[3] Spencer, B.F., Ruiz-Sandoval, M.E. and Kurata, N., 2004, "Smart Sensing Technology: Opportunities and Challenges," Structural Control and Health Monitoring, 11(4) pp.349-368.

[4] V. Leonov, T. Torfs, P. Fiorini, and C. Van Hoof, Thermoelectric Converters of Human Warmth for SelfPowered Wireless Sensor Nodes, IEEE Sensors Journal, vol. 7, N. 5, May 2007.

[5] Raghunathan, V., Kansal, A., Hsu, J., Friedman, J. and Srivastava, M.. "Design considerations for solar energy harvesting wireless embedded systems". In IPSN '05: Proceedings of the 4th international symposium on Information processing in sensor networks, page 64, Piscataway, NJ, USA, 2009. IEEE Press.

[6] STMicroelectronics- STM32L- Ultra Low Power 32-bit Microcontroller www.st.com/STM32L

[7] S. Roundy, E.S. Leland, J. Baker, E. Carleton, E. Reilly, E. Lai, B. Otis, J.M. Rabaey, P.K. Wright, V. Sundararajan, IEEE Pervasive Computing 4, 28 (2005)

[8] H.-C. Kim, D.-Y. Jeong, S.-J. Yoonm, H.-J. Kim, Kor. J. Mater." Low Power Operation of 32-bit Microcontrollers" Res. 17, 121 (2007)

[9] STMicroelectronics, MEMS in portable applications. Available on: http://st.com/advanced_analog/MEMS/AN751.pdf. Accessed May 15, 2012

[10] Clarence W. de Silva: "Sensors and Actuators-Control System Instrumentation", page 64, CRC Press, Taylor & Francis Group, New York, 2011

[11] STMicroelectronics, LIS33DLH datasheet. 28/40/44-Pin flash-based, Ultra Low Power Accelerometer. Available on: http://www.st.com/MEMS downloads/en/DeviceDoc/41341C.pdf. Accessed 2012

[12] ST Technology for Healthcare Innovation: "Gyro(LY530AL, LISY300AL)" Available on: http://www.st.com/MEMS. Accessed 2012

[13] ST Technology for Cyber Physical and motion sensing: "Magnetometer (LSM303DLM)" Available on: http://www.st.com/MEMS . Accessed 2012

[14] ST Technology for Cyber Physical and motion sensing: “Pressure Sensor (LPS001WP)”. Available on the www.st.com/MEMS. Accessed 2012

[15] STMicroelectronics Ultra Low Power Digital Temperature Sensor

Available on: http://www.st.com/temperaturesensors. Accessed 2012

[16] STMicroelectronics: “Dual Interface EEPROM”. Available on:

www.st.com/dual_nfc_androidappli.pdf

Accessed 2012

[17] 15. Dove, J.R., Park, G. and Farrar, C.R., 2005, “Hardware Design of Hierarchal Active-Sensing Networks for Structural Health Monitoring,” Smart Materials and Structures, 15, pp. 139-146.

[18] Tanner, N.A., Wait, J.R., Farrar, C.R. and Sohn, H., 2003, “Structural Health Monitoring using Modular Wireless Sensors, *Journal of Intelligent Material systems and Structures*, **14**(1) pp. 43-56.

[19] Miao, P.; Mitcheson, P. D.; Holmes, A. S.; Yeatman, E. M.; Green, T. C. and

Stark, B. H. MEMS inertial power generators for biomedical applications.

Microsyst. Technol., 12(10-11), 2006, pp. 1079-1083.

[20] Myers, G. H.; Parsonnet, V.; Zucker, I. R.; Lotman, H. A. and Asa, M. M.

Biologically-energized cardiac pacemaker. IRE transactions on bio-medical

electronics, 10(2), 1963, p. 83.

[21] M. Conner, Run for your life: Ultra-low power systems designed for the long Haul.EDN, electronic design newsletter (2005, April 2010). Available on: http://www.edn.com/article/ 471243Run_for_your_life_Ultralow_power_systems_designed_for_the_long_haul.php

[22] Chulsung Park and Pai H. Chou. AmbiMax: Efficient, autonomous energy harvesting system for multiple esupply wireless sensor nodes. In Proceedings of the Third Annual IEEE Communications Society Conference on Sensor, Mesh, and Ad Hoc Communications and Networks (SECON), pages 168–177, Reston, VA, USA, September 25–28 2006.

[23] T. STARNER AND J.A. PARADISO, "HUMAN- GENERATED POWER FOR MOBILE ELECTRONICS," LOW-POWER ELECTRONICS DESIGN, C. PIGUET, ED., CRC PRESS, 2004, CHAPTER 45, PP. 1–35.

[24] E.M. YEATMAN, "ADVANCES IN POWER SOURCES FOR WIRELESS SENSOR NODES," PROC. INT'L WORKSHOP WEARABLE AND IMPLANTABLE BODY SENSOR NETWORKS, IMPERIAL COLLEGE, 2004, PP. 20–21; WWW.DOC.IC.AC.UK/VIP/ BSN_2004/PROGRAM/INDEX.HTML.

[25] SHASHANK PRIYA · DANIEL J. INMAN "ENERGY HARVESTING TECHNOLOGIES" (SPRINGER SCIENCE+BUSINESS MEDIA, LLC, 233 SPRING STREET, NEW YORK, NY 10013, USA, PG .65

[26] Davide Brunelli, Luca Benini, Clemens Moser, and Lothar Thiele. An efficient solar energy harvester for wireless sensor nodes. In *Proc. Design,* Automation and Test in Europe Conference and Exhibition (DATE), 2008.

[27] Li, X., Guo, M. and Dong, S., "A flex-compressive-mode piezoelectric transducer for mechanical vibration/strain energy harvesting," IEEE Transactions on Ultrasonics, Ferroelectrics and Frequency Control, Vol. 58, No. 4, pp. 698-703, 2011.

[28] Marzencki, M., Defosseux, M. and Basrour, S., "MEMS vibration energy harvesting devices with passive resonance frequency adaptation capability," Journal of Microelectromechanical Systems, Vol. 18, No. 6, pp. 1444- 1453, 2009.

[30] Clarence W. de Silva: " Sensors and Actuators- Control System Instrumentation"

CRC Press, Taylor & Fracis Group, New York, 2007 pg. 238

[31] D. Patranabis, Sensors and Transducers, 2nd edition, PHI Learning, PVT, Englewood Cliffs, N.J. 2001

[32] Beeby, et al, *Measurement Science and Technology*, **17**, R175-R195 (2006)

[33] Shu, Y. C. and Lien, I. C., "Efficiency of energy conversion for a piezoelectric power harvesting system," Journal of Micromechanics and Micro Engineering, Vol. 16, No. 11, pp. 2429-2438, 2006.

[34] Marzencki, M., Defosseux, M. and Basrour, S., "MEMS vibration energy harvesting devices with passive resonance frequency adaptation capability," Journal of Microelectromechanical Systems, Vol. 18, No. 6, pp. 1444- 1453, 2009.

[35] V. Leonov, T. Torfs, P. Fiorini, and C. Van Hoof, Thermoelectric Converters of Human Warmth for SelfPowered Wireless Sensor Nodes, IEEE Sensors Journal,

vol. 7, N. 5, May 2007.

[36] www.micropelt.com.

[37] D. Morton. *Human Locomotion and Body Form.* The Williams & Wilkins Co., Baltimore, MD, 1952.

[38] V. Leonov, T. Torfs, P. Fiorini, and C. Van Hoof, Thermoelectric Converters of Human Warmth for SelfPowered Wireless Sensor Nodes, IEEE Sensors Journal, vol. 7, N. 5, May 2007.

[39] Bogus, Klaus and Markvart, Tomas. Solar Electricity. Chichester, New York.

Wiley Press, 2005.

[40] Nation Center for Photovoltaic's. "Turning Sunlight into Electricity." 20 Oct. 2007.

<http://www.eren.doe.gov/pv/siatomic.html>.

[41] B.-r. Chen, "LEGSys: wireless gait evaluation system using wearable sensors," *Proceedings of the 2nd Conference on Wireless Health*, San Diego, California, 2011.

[42] A. T. Barth, M. A. Hanson, H. C. Powell, and J. Lach, "TEMPO 3.1: A Body Area Sensor Network Platform for Continuous Movement Assessment," *Proceedings of the 6th International Workshop on Wearable and Implantable Body Sensor Networks,* 2009, pp. 71-76.

[43] B. Najafi, T. Khan, and J. Wrobel, "Laboratory in a box: Wearable sensors and its advantages for gait analysis," *Proceedings of the IEEE Engineering in Medicine and Biology Society Annual Conference*, pp. 6407-6510, 2011.

[44] H. Vathsangam, A. Emken, D. Spruijt-Metz, and G. S. Sukhatme, "Toward free-living walking speed estimation using Gaussian Process-based Regression with on-body accelerometers and gyroscopes," *Proceedings of the 4th International Conference on Pervasive Computing Technologies for Healthcare (PervasiveHealth)*, 2010, pp. 1-8.

[45] S. Yoonseon, S. Seungchul, K. Seunghwan, L. Doheon, and K. H. Lee, "Speed Estimation From a Tri-axial Accelerometer Using Neural Networks," *Proceedings of the*

IEEE Engineering in Medicine and Biology Society Annual Conference, 2007, pp. 3224-3227.

[46] . Ravi, N. Dandekar, P. Mysore, and M. L. Littman, "Activity recognition from accelerometer data," *Proceedings of the 17th conference on Innovative applications of artificial intelligence*, Pittsburgh, Pennsylvania, 2005.

[47] J. Suutala, S. Pirttikangas, and J. Röning, "Discriminative Temporal Smoothing for Activity Recognition from Wearable Sensors," *Ubiquitous Computing Systems*, vol. 4836, 2007, pp. 182-195

[48] Z. Zilic and K. Radecka, "Fault Tolerant Glucose Sensor Readout and Recalibration," *Proceedings of the 2nd Conference on Wireless Health*, San Diego, California, 2011. pp. 169 – 170.

[49] A. Giordano and F. M. Hsu. *Least Square Estimation with Applications to Digital Signal Processing*, New York, NY, USA: John Wiley & Sons, Inc.,1985.

[50] L. B. Jackson, *Digital Filters and Signal Processing*, Norwell MA: Kluwer Academic Publishers, 1996, pp. 290-313.

[51] S. P. Tseng, L. Wen-Lung, S. Chih-Yang, H. Jia-Wei, and C. Chin-Sheng, "Motion and attitude estimation using inertial measurements with complementary filter," in *Proceedings of the 8th Asian Control Conference (ASCC)*, 2011, pp. 863-868.

[52] Ceraolo, M. (2000) \New Dynamical Models of LeadAcid Batteries," IEEE Transactions On Power Systems, 15, p. 1184.

[53] Scherson, D. A. and A.Palencsar (2006) \Batteries and Electrochemical Capacitors," Electrochem. Soc. Interface, pp. 17{22.

[54] K. E. Thomas, J. S. Newman, and R. M. Darling, "Advances in Lithium-ion Batteries", Walter A. van Schalkwijk and Bruno Scrosati, p. 362 (2002)

[55] Srinivasan, V. and J. W. Weidner (1999) \Mathematical Modeling of Electrochemical Capacitors," Journal of The Electrochemical Society, 146, pp. 1650{1658.

[56] Nano Markets Report, Thin-Film and Printed Batteries Market, White Paper, March 2008, www. nanomarkets.net

[57] S.D. Fabre, D. Guy-Bouyssou, P. Bouillon, F. Le Cras and C. Delacourt, Charge/Discharge Simulation of an All-Solid-State Thin-Film Battery Using a One-Dimensional Model, *J. Electrochem. Soc.* 2011, Volume 159, Issue 2, Pages A104-A115.

[58] eDesignSuite Online Design Circuit Simulator by STMicroelectronics. Available at www.st.com/internet/com/software/edesignsuite.jsp

[59] V. Gourishankar and D. H. Kelly, *Electromechanical Energy Conversion,* New York: Intext Educational Publishers, 1973.

[60] N. Lobontiu, *Mechanics of Microelectromechanical Systems,* Springer, 2004.

[61] L. Tvedt, L. Blystad, and E. Halvorsen, “Simulation of an electrostatic energy harvester at large amplitude narrow and wide band vibrations,” *Simulation,* vol. 9, p. 5-11, 2008.